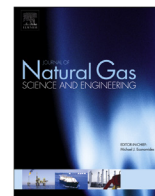




Contents lists available at ScienceDirect

## Journal of Natural Gas Science and Engineering

journal homepage: [www.elsevier.com/locate/jngse](http://www.elsevier.com/locate/jngse)

## Lithofacies and pore characterization of the Lower Permian Shanxi and Taiyuan shales in the southern North China Basin

Shuai Tang<sup>a, b, c</sup>, Jinchuan Zhang<sup>a, b, \*</sup>, Derek Elsworth<sup>c</sup>, Xuan Tang<sup>a, b</sup>, Zhongming Li<sup>d</sup>, Xiaorui Du<sup>a, b</sup>, Xiaoqun Yang<sup>a, b</sup><sup>a</sup> Key Laboratory of Shale Gas Exploration and Evaluation, Ministry of Land and Resources, China University of Geosciences, Beijing 100083, China<sup>b</sup> School of Energy Resources, China University of Geosciences, Beijing 100083, China<sup>c</sup> College of Earth and Mineral Sciences, The Pennsylvania State University, University Park, PA 16802-5000, USA<sup>d</sup> Henan Institute of Geological Survey, Zhengzhou 450000, China

## ARTICLE INFO

## Article history:

Received 3 May 2016

Received in revised form

3 November 2016

Accepted 4 November 2016

Available online 5 November 2016

## Keywords:

Shale gas

Mineral composition

Total organic carbon

Nitrogen gas adsorption

Fracturing target

Southern North China Basin

## ABSTRACT

Marine-continental transitional shales with varied lithofacies are widely distributed in the Lower Permian Shanxi and Taiyuan Formations in the southern North China Basin (sNCB) where they have been subject to frequently changing depositional conditions. Despite their importance, integrative classifications of the lithofacies of such shales are not normalized primarily due to the complex composition of the formations. This work classifies and defines the pore microstructure of the Shanxi and Taiyuan shales (well Mouye-1) from the Zhongmou exploration area. Classification is performed by optical (polarizing) microscopy, X-ray diffraction, and scanning electronic microscopy (SEM) imaging of Ar-ion milled samples, yielding measurements of the total organic carbon (TOC) content, porosity, and nitrogen adsorption. The TOC content is introduced into traditional ternary plots denoting “clay-carbonate-quartz”. Four primary lithofacies are identified from the combined metrics of optical microscopy and inorganic and organic contents. These four divisions comprise silt bearing mudstones, silty mudstones, muddy siltstones, and silty carbonaceous mudstones. The samples exhibit porosities between 1% and 4.5%, with silty carbonaceous mudstones having the highest TOC content and returning the highest porosity. Pores hosted in both the inorganic matrix and organic substrate are imaged by SEM. The predominant and largest pore types are in the inorganic matrix and include inter-particle mineral pores, inter-crystalline mineral pores and secondary denudation pores caused by smectite illitization. The pore size distributions (PSDs) and specific surface areas are recovered from nitrogen gas adsorption using BJH and BET models that reveal a wide range of pore sizes. The pore volumes are predominately associated with larger macro-/mesopores, whereas the specific surface area is primarily from a contribution of smaller micro-/mesopores. Finally the target zone for fracturing and recovery is optimized using these integrated methods for lithofacies description, pore characterization, and petrophysical and geo-mechanical analysis. This study provides a selective completion strategy to reduce fracturing-treatment expense and improve well productivity.

© 2016 Elsevier B.V. All rights reserved.

## 1. Introduction

Significant progress has been made in the exploration and development of unconventional shale gas worldwide, especially in

North America (Wang and Carr, 2012). The expanded application of horizontal drilling and hydraulic fracture stimulation technology has been shown to be capable of recovering gas at economic and industrial flow rates from unconventional resources that have extremely low porosity and permeability (Mitra et al., 2010). Previous research on lithofacies characterization primarily focused on sandstone and carbonate reservoirs, using descriptions from core data and outcrops (Bridge et al., 2000; Porta et al., 2002). The prediction of lithofacies using logging techniques, seismic volume (Berteig et al., 1985; Wong et al., 1995; Qi and Carr, 2006), and

\* Corresponding author. School of Energy Resources, China University of Geosciences, Beijing 100083, China.

E-mail addresses: [tangshuaier@163.com](mailto:tangshuaier@163.com) (S. Tang), [452224822@qq.com](mailto:452224822@qq.com) (J. Zhang), [elsworth@psu.edu](mailto:elsworth@psu.edu) (D. Elsworth), [tangxuan@cugb.edu.cn](mailto:tangxuan@cugb.edu.cn) (X. Tang), [771219188@qq.com](mailto:771219188@qq.com) (Z. Li), [653005823@qq.com](mailto:653005823@qq.com) (X. Du), [yxq@cugb.edu.cn](mailto:yxq@cugb.edu.cn) (X. Yang).

lithofacies modeling in two and three dimensions (Akatsuka, 2000; Yao and Chopra, 2000; Qi et al., 2007) has been well developed for conventional reservoirs. However, lithofacies studies of shales are in their infancy (Zhang et al., 2008; Javadpour, 2009; Curtis et al., 2010; Aplin and Macquaker, 2011; Loucks et al., 2012). As a result, primarily due to the complex composition of the formations, such nascent integrative classifications for shales have not been normalized. In this study, the content of “total organic carbon (TOC)” is introduced into traditional ternary plots of “clay-carbonate-quartz”, defining a new tri-partite lithofacies classification based on the relative contents of different minerals. Such a classification of shales aids in design optimization of horizontal wells and stimulation strategies in unconventional reservoirs, where the porosity-permeability characteristics correlate with different lithofacies.

Compared with conventional sand and carbonate reservoirs, shale gas systems, where the unit serves as both source rock and reservoir rock (Jarvie et al., 2007; Hill et al., 2007), exhibit extremely low porosity and permeability (Curtis et al., 2010; Javadpour, 2009). Gas is stored in any of three forms: free gas in pores and fractures, gas adsorbed onto the surface of organic and inorganic matter and gas dissolved in oil and water (Curtis, 2002; Zhang et al., 2004). Pore shapes and extents can be observed by Broad Ion Beam-Scanning electron microscopy (BIB-SEM) (Houben et al., 2013; Klaver et al., 2012, 2015; Yang et al., 2014). This technique can be used to determine the shapes and sizes of pores as a complementary technique in combination with the quantification of the pore structure and pore size distribution derived from Nitrogen Gas Adsorption ( $N_2GA$ ) (Loucks et al., 2009; Mayka et al., 2013; Milliken et al., 2013). Traditional methods of helium porosimetry (Bustin et al., 2008; Chalmers et al., 2012a) can establish a combined PSD and total porosity, but they are difficult to apply to shales due to the complexity of the pore network microstructures (Curtis et al., 2012; Nelson, 2009) – thus, alternate methods must be used to characterize pore morphology.

Marine shales in southern China have received renewed attention during the past few years, similar to the renewed interest in marine strata in the United States (Zeng et al., 2012; Tian et al., 2013; Wu et al., 2014; Dong et al., 2015; Yang et al., 2016). However, studies associated with transitional gas shales in northern China, which differ significantly from marine shales in terms of the conditions of gas accumulation and organic geochemical characteristics, remain rare (Ding et al., 2013). Since the petrophysical and geomechanical properties vary abruptly both vertically and laterally, the recovery of gas from shales using traditional hydraulic fracturing techniques is significantly influenced by the heterogeneity of the target zone (Boyer et al., 2006). In this study, 35 samples from the Lower Permian Shanxi and Taiyuan Formations (southern North China Basin, Henan Province (Mouye-1 well)) are characterized for lithofacies and pore characteristics. These characterizations include measurements of the inorganic mineral composition, organic geochemical parameters, pore morphology, pore microstructure, total porosity and mechanical properties. The major objectives of this study are to: (1) describe and classify the lithofacies of the Lower Permian Shanxi and Taiyuan Formations through according to their inorganic mineral composition and total organic carbon content; (2) investigate the pore characteristics, such as the porosity, pore types, pore size distribution and specific surface area; and (3) identify the potential target zone for hydraulic fracturing and production by using these integrated data.

## 2. Geologic setting

The southern North China Basin (sNCB) is located at the junction between the southern part of the North China plate and the

southern Qinling-Dabie orogenic belt (Yu et al., 2005; Huang et al., 2005). This belt has a unique and complex tectonic history resulting from its special geotectonic location. The sNCB has experienced long-term multiphase tectonic movements, including compressional thrust tectogenesis (during the Indo-Chinese epoch), strike-slip stretching tectogenesis (during the Yanshan epoch), and extensional faulting depression (during the Xishan epoch). The mutual superposition and reconstruction of these tectonic movements are closely related to oil and gas exploration since they control the preservation and distribution of Permo-Carboniferous hydrocarbon resources in the sNCB (Xu et al., 2004; Lv et al., 2005). The sNCB was developed during the Mesozoic Indo-Chinese epoch and is further divided into five secondary tectonic units. These include the Kaifeng depression, Taikang uplift, Zhoukou depression, Bengbu uplift and Xinyang-Hefei depression (Fig. 1) (Sun, 1996; Wang et al., 1994).

The Zhongmou exploration area lies in the southwest part of the Kaifeng depression and together with the northwest part of the Taikang uplift belongs to the “Mesozoic-uplift & Cenozoic-depression” tectonic evolution pattern. The Lower Permian strata, which comprise the Taiyuan, Shanxi, Lower Shihezi, Upper Shihezi, Pingdingshan and Sunjiagou formations, have been recognized as effective source rock within the research area. However, the Taiyuan and Shanxi Formations are the two major exploration targets, in which the Taiyuan Formation represents transitional deposition from marine to continental facies. Thus it contains lithofacies of mudstone, limestone, sandstone and coal beds resulting from inter-tidal sedimentation to a thickness of 39–140 m. The Shanxi Formation is a delta sedimentary system of tidal, lagoon, peat bog and delta deposits with a thickness of 73–103 m and is dominated by sandstones, sandy mudstones, mudstones and coal beds (Fig. 2). The alternating variation of four different lithologies, including mudstone/shale, coal, sandstone, and limestone, in the Shanxi and Taiyuan Formations of the Lower Permian reflect frequent changes in depositional conditions (Qin, 2005; Zou et al., 2010). Well logs (Fig. 2.) show moderate to high gamma intensity and high resistivity readings for shale, low gamma intensity and high resistivity for coal, low gamma intensity for sandstone and extremely low gamma intensity for limestone. Kerogens in the shales of the two formations are predominantly humic (type III), showing their promising prospect for shale gas.

The Mouye-1 exploration well probes the Lower Permian Shanxi and Taiyuan Formations shales in the Zhongmou exploration area. The exploration well is fully cored throughout these two formations to evaluate the characteristics of the transitional shale gas reservoir in this region via geochemical, mineralogical, petrological, petrophysical and pore microstructural characterization methods and to relate these characteristics to gas potential.

## 3. Methodology

### 3.1. Samples

A total of thirty-five core samples from the Lower Permian Shanxi and Taiyuan Formations shales were collected from the Mouye-1 well at depths of 2806.36–2963.00 m using sampling intervals of ~2–3 m. These contained 19 black shale intervals with thicknesses of ~2–8 m (Fig. 2). Detailed information for each shale sample involved, including the stratigraphy, lithology, sample location, and log data, is shown in Fig. 2.

### 3.2. Methods

The samples were characterized for their geochemical, mineralogical, petrological, petrophysical and pore microstructural

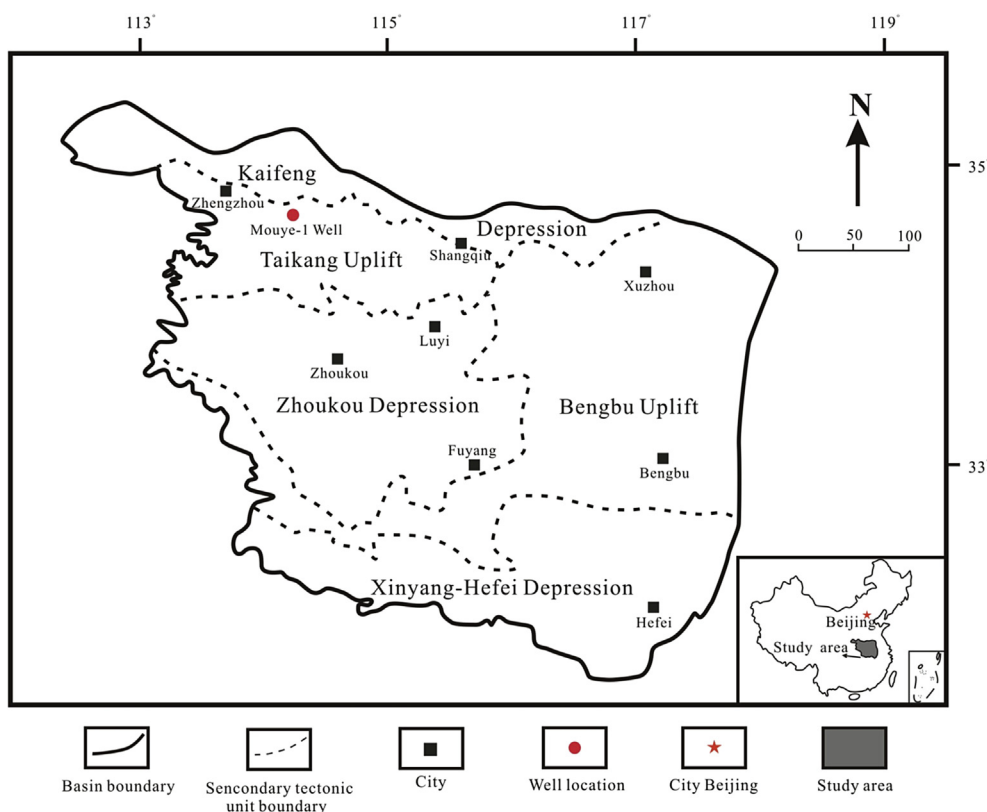


Fig. 1. Simplified structural map of the southern North China Basin, showing well locations (modified from Sun, 1996).

characteristics using a variety of techniques.

### 3.2.1. Polarizing microscopy

An Olympus CX31-P polarizing microscope was used for preliminary observation of the micro-distribution of organic matter in collected samples via thin sections. This was conducted following the criteria of the Chinese standard SY/T 5368–2000, 2000.

### 3.2.2. X-ray diffraction (XRD)

Thirty-five shale samples were crushed into powder for X-ray diffraction (XRD) using a Bruker D8 Advance X-Ray Diffractometer at 40 kV and 30 mA with Cu K $\alpha$  radiation ( $\lambda = 1.5406$  for CuK $\alpha$ 1). Stepwise scanning measurements were performed at a rate of 4°/min in the range of 3°–85° (2 $\theta$ ). Measured data were then analyzed qualitatively using EVA (Bruker) software and estimated semi-quantitatively using the method of weight coefficients (Chalmers and Bustin, 2008). All mineral assays are given as a weight percent (wt.%) on the basis of the Chinese Oil and Gas Industry Standard SY/T 5163–2010, 2010.

### 3.2.3. Organic geochemistry

The total organic carbon (TOC) of the 35 samples was determined using a Leco CS230 carbon/sulfur analyzer in accordance with the Chinese standard (GB/T19145–2003, 2003). Samples were first crushed to powder with a particle size <100 mesh, with a minimum mass of 10 g. Excess dilute hydrochloric acid was used to remove carbonates from the measured samples. After rinsing and drying, the de-carbonated samples were reweighed and pyrolyzed at high temperatures in a Leco CS230. Finally, the organic carbon content of each sample was acquired as a weight percentage through comparison with a calibration sample of a known standard value.

Basic parameters, including the volatile hydrocarbon content (S1), remaining hydrocarbon generative potential (S2) and temperature of maximum pyrolysis yield (Tmax), were measured for the 35 samples using a Rock-Eval 6 instrument at 600 °C. Tmax was used to calculate the vitrinite reflectance (%Ro) (Jarvie and Lundell, 1991; Jarvie et al., 2001). To guarantee the reliability of the calculated Ro values, vitrinite reflectance values of 18 samples were also measured using a MPV-SP microphotometer under oil immersion (Chinese standard SY/T5124–1995, 1995). The primary maceral compositions were also measured with an optical microscope under reflected white and fluorescent light according to the Chinese standard SY/T5125–1996, 1996.

### 3.2.4. Pore characterization

A Helium pycnometer was used to measure the skeletal density to further calculate the porosity in combination with mass measurements (i.e., the weight of the sample in air; the weight of the sample sealed by paraffin with known density in air, and the weight of the paraffin-sealed sample in water) (Ling et al., 2011; Wang et al., 2005; Chalmers et al., 2012a; Gasparik et al., 2014).

BIB-SEM was used to observe the shapes of the pores in the shale samples (Klaver et al., 2012, 2015; Houben et al., 2013). The samples were prepared by Argon ion-milling to create a smooth surface using a Hitachi IM4000 miller with an accelerator voltage of 3 kV and a milling time of 4 h. Ion-milled samples were then imaged by a scanning electron microscope (SEM) to measure the matrix components, organic matter, and pore sizes and shapes. Secondary electron images documented topographic variation, and back scattered electron (BSE) images delineated compositional variation (Hitachi S4800 and FEI Helios NanoLab™ 600 systems). Lower accelerator voltages of 5 kV with working distances of 8–10 mm were typically used on these systems to prevent beam

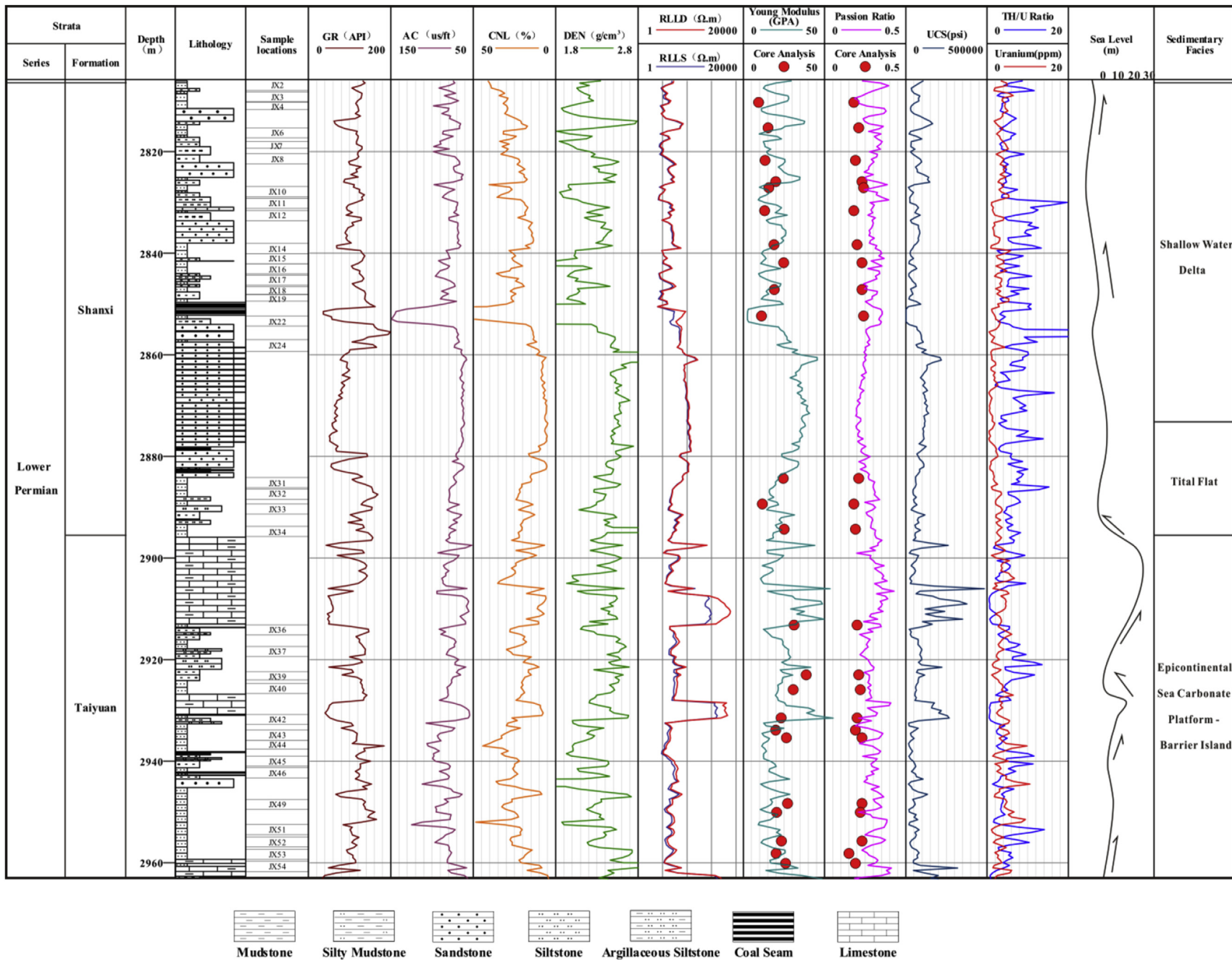
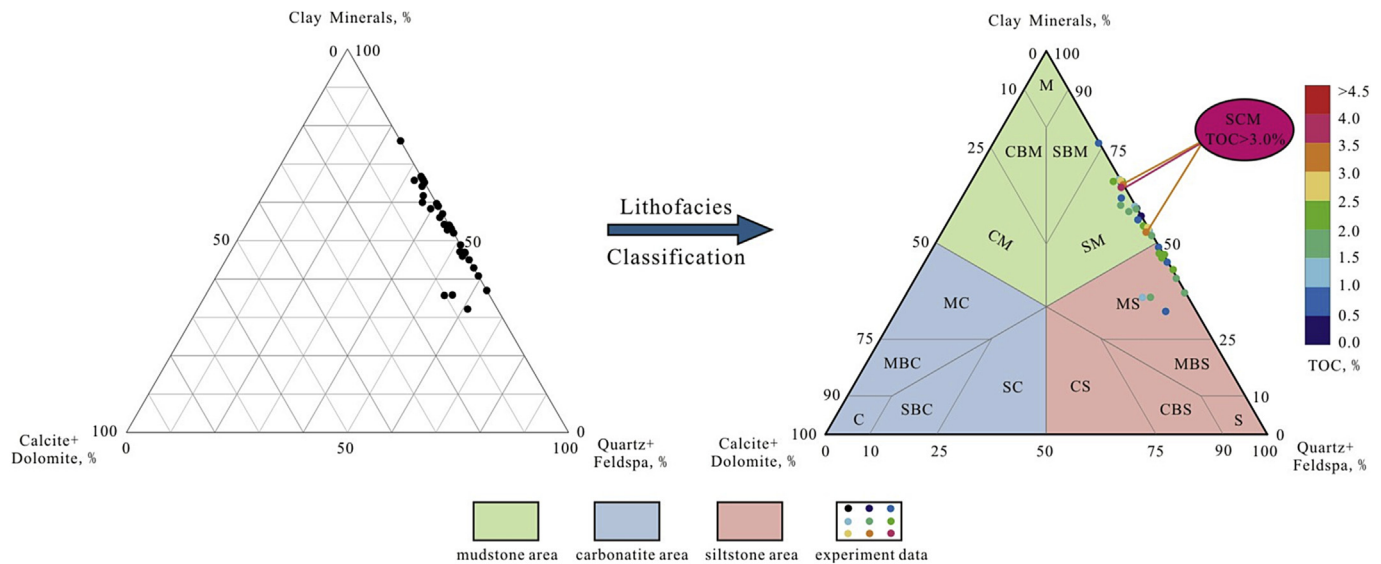


Fig. 2. Generalized lithological variations and log data of the Lower Permian Shanxi and Taiyuan Formation, associated with locations of core samples collected from well Mouye-1 (modified from Chen et al., 1997). Core Analysis data represent the Young's modulus and Poisson ratios derived from triaxial compression tests.

**Table 1**  
Inorganic Mineral Composition and Total Organic Carbon of Shanxi and Taiyuan formation core samples.

Sample	Depth (m)	Formation	Quartzz(%)			Carbonates(%)			Clay (%)	TOC (%)
			Quartz	Feldspar	Total	Calcite	Dolomite	Total		
JX2	2804.81	P1s	31	2	33	0	0	0	67	1.0
JX3	2807.74	P1s	24	0	24	0	0	0	76	0.8
JX4	2810.32	P1s	50	3	53	0	0	0	47	0.6
JX6	2815.3	P1s	51	0	51	0	0	0	49	1.0
JX7	2819.27	P1s	32	2	34	0	0	0	66	2.0
JX8	2821.74	P1s	35	6	41	0	0	0	59	0.5
JX10	2827.13	P1s	34	0	34	0	0	0	66	0.7
JX11	2830.72	P1s	41	12	53	0	0	0	47	2.1
JX12	2831.66	P1s	35	5	40	0	0	0	60	1.1
JX14	2838.32	P1s	40	3	43	0	0	0	57	0.4
JX15	2840.23	P1s	40	8	48	0	0	0	52	1.7
JX16	2841.88	P1s	43	3	46	0	0	0	54	2.6
JX17	2844.32	P1s	42	5	47	0	0	0	53	1.2
JX18	2847.16	P1s	43	4	47	0	0	0	53	0.5
JX19	2848.82	P1s	29	7	36	0	2	2	62	0.8
JX22	2852.36	P1s	59	4	63	0	0	0	37	1.9
JX24	2857.02	P1s	43	3	46	0	0	0	54	2.7
JX31	2884.3	P1s	57	2	59	0	0	0	41	1.7
JX32	2886.27	P1s	38	3	41	0	0	0	59	1.5
JX33	2889.34	P1s	50	7	57	0	0	0	43	2.1
JX34	2894.31	P1s	35	2	37	0	3	3	60	1.8
JX36	2913.2	P1t	41	5	46	0	1	1	53	3.0
JX37	2917.42	P1t	31	3	34	0	0	0	66	2.6
JX39	2923	P1t	48	4	52	0	1	1	47	2.3
JX40	2925.92	P1t	41	4	45	0	1	1	54	2.4
JX42	2931.5	P1t	29	3	32	0	2	2	66	2.5
JX43	2933.86	P1t	35	0	35	0	1	1	64	3.6
JX44	2935.4	P1t	49	4	53	0	1	1	46	2.2
JX45	2939.27	P1t	38	2	40	1	1	2	58	1.8
JX46	2941.28	P1t	55	0	55	0	0	0	45	0.6
JX49	2948.32	P1t	35	0	35	0	0	0	65	3.0
JX51	2953.09	P1t	53	3	56	5	3	8	36	1.9
JX52	2955.71	P1t	61	0	61	0	6	7	32	1.0
JX53	2958.16	P1t	51	3	54	0	10	10	36	1.1
JX54	2960.13	P1t	39	4	43	1	0	1	56	0.8

P<sub>1s</sub> = Lower Permian Shanxi formation; P<sub>1t</sub> = Lower Permian Taiyuan formation; Quartz = Quartz + Feldspa; Carbonates = Calcite + Dolomite; TOC = total organic carbon.



**Fig. 3.** Lithofacies classification ternary diagram with mineral compositions and overlain by TOC for Shanxi and Taiyuan shales collected from well Mouye-1 based on Table 1 (modified from Dong et al., 2015).

M = Mudstone; S=Siltstone; C=Carbonate = Calcarenite(calcite content > dolomite content)/Dolomite(dolomite content > calcite content); SM=Silty Mudstone; CM=Calcareous Mudstone/Dolomite Mudstone; MS = Muddy Siltstone; CS=Calcareous Siltstone/Dolomite Siltstone; MC = Muddy Calcareous/Muddy Dolomite; SC=Silty Calcareous/Silty Dolomite; SBM=Silt Bearing Mudstone; CBM=Calcite Bearing Mudstone/Dolomite Bearing Mudstone; MBS = Mud Bearing Siltstone; CBS=Calcite Bearing Siltstone/Dolomite Bearing Siltstone; MBC = Mud Bearing Calcareous/Mud Bearing Dolomite; SBC=Silty Bearing Calcareous/Silty Bearing Dolomite; SCM=Silty Carbonaceous Mudstone; TOC = Total Organic Carbon.

damage to the samples.

Low pressure nitrogen adsorption was conducted to elucidate the complex pore system, including the specific surface areas and pore size distributions, based on BET and BJH models (Brunauer et al., 1938; Barret et al., 1951; Mastalerz et al., 2012; Kuila and Prasad, 2013). In this study, samples were crushed and sieved to a 60–80 mesh size (mass between 0.6383 and 0.9538 g), dried in an oven at 110 °C for 12 h and then degassed under high vacuum (<10 mmHg), typically for 10 h at 150 °C. A nitrogen vapor pressure thermometer was used to determine the saturation vapor pressure ( $p_0$ ) of  $N_2$  at 77 K every 120 min. The relative pressure ( $p/p_0$ ) ranged from 0.012 to 0.993 during the analysis with an applied equilibration time of 10 s. Low pressure nitrogen adsorption isotherms were obtained at 77 K on an accelerated surface area and porosimetry system - BK132F. The specific surface area and pore size analysis followed the Chinese standard GB/T19587-2004 and Chinese Oil and Gas Industry Standard SY/T6154-1995.

### 3.2.5. Geomechanical experiments

Triaxial compression tests were performed on 23 samples using

a WEP-600 servo-hydraulic rock testing system with digital feedback control (Britt and Schoeffler, 2009). All specimens were jacketed with a 0.5-mm thick DuPont FEP Fluorocarbon Film, and all tests were executed with impervious end plates. Young's Modulus and Possion's Ratio were obtained to assess rock brittleness. The two components were first binned into their different units and then averaged to yield the brittleness index as a percentage, using (Rickman et al., 2008):

$$YM_{BI} = (\text{Young's Modulus} - 1) / (8 - 1) \times 100\% \quad (1)$$

$$PR_{BI} = (\text{Possion's Ratio} - 0.4) / (0.15 - 0.4) \times 100\% \quad (2)$$

$$BI = (YM_{BI} + PR_{BI}) / 2 \quad (3)$$

where  $YM_{BI}$  is the binned Young's Modulus,  $PR_{BI}$  is the binned Possion's Ratio, and BI is the brittleness index.

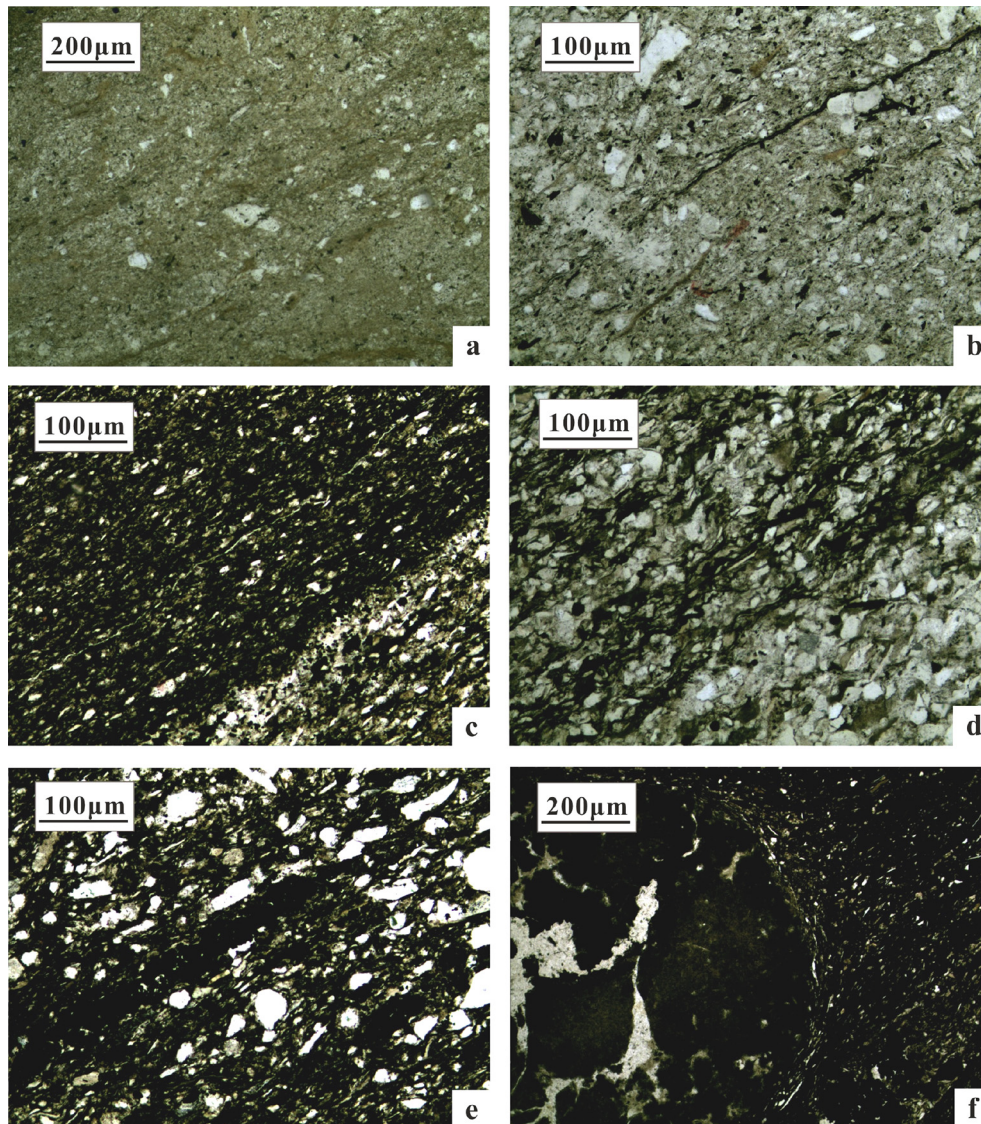


**Fig. 4.** Thin-section lithofacies of shale samples from the Shanxi and Taiyuan Formations: (a) SBM (JX3), 200 × ; (b) SM (JX14), 100 × ; (c) SM (JX42), 100 × ; (d) MS (JX31), 100 × ; (e) MS (JX44), 100 × ; (f) SCM (JX36), 200 × , TOC>3.0%.

## 4. Results

### 4.1. Lithofacies classification

The mineral compositions and TOC contents of the 35 core samples are listed in Table 1. Based on these data and thin-section examination, a ternary diagram composed of mineral compositions and TOC contents (Fig. 3) was used to divide the Lower Permian Shanxi and Taiyuan Formation shales into four lithofacies:

#### 4.1.1. Silt bearing mudstone (SBM)

The thin-section microphotograph of JX3 is the type-example for SBM (Fig. 4a). Mica and a clastic matrix with a small amount of recrystallization constitute the argillaceous components. The heterogeneously distributed quartz and feldspar and directionally distributed mica particles constitute the banded sandy components. The TOC content of this lithofacies is the lowest at 0.78% (Fig. 5).

#### 4.1.2. Silty mudstone (SM)

SM samples with a silty argillaceous texture were the dominant lithofacies of the core samples collected from Mouye-1 (Fig. 4b and c). The argillaceous components were primarily composed of mica and clastic matrix. The sandy components were primarily composed of quartz, feldspar, argillic particles, mica, and some carbonatite fragments. Carbonaceous matter was fragmentally present in layered or mixed distribution. Unfilled bed-parallel micro-cracks were present (Fig. 4b), and small amounts of pyrite were randomly distributed (Fig. 4c). SM had a relatively higher TOC content ranging from 0.47% to 2.69%, with an average value of 1.45% (Fig. 5).

#### 4.1.3. Muddy siltstone (MS)

MS samples generally exhibited an argillaceous and sandy lamellar texture. The argillaceous components consisted of clastic

matrix and mica. The sandy components were primarily comprised of quartz, feldspar, argillic particles and mica. Carbonaceous matter was distributed as bands or as distributed fragments, whereas micritic siderite was speckled throughout. Pyrite was present as bands or as porphyritic shapes (Fig. 4e). Unfilled micro-cracks were parallel to the bedding strata (Fig. 4d). MS had higher TOC contents ranging from 0.56% to 2.31%, with an average value of 1.53% (Fig. 5).

#### 4.1.4. Silty carbonaceous mudstone (SCM)

SCM with a silty argillaceous texture was uniformly mixed with carbonaceous matter (Fig. 4f). The argillaceous components were primarily comprised of clastic matrix and mica. The sandy components were unevenly distributed and micro-bedded with the main constituents of a small quantity of quartz, feldspar, argillic particles and mica. Pyrite was distributed in bands or as porphyritic shapes concentrated in massive blocks with siderite and sericite and always surrounded by sand and mud. Unfilled micro-cracks were developed parallel to the bedding strata. This lithofacies had the highest TOC content ranging from 3.02% to 3.56%, with an average of 3.21% (Fig. 5).

### 4.2. Organic geochemical parameters

The Rock-Evaluation results and maceral compositions of the shale samples from the Shanxi and Taiyuan formations are listed in Table 2. They make it impossible to calculate the vitrinite reflectance and identify the kerogen type (Jarvie et al., 2001; Hou and Feng, 2011). Based on maceral compositions, the type index (TI) was introduced to determine the kerogen types (Cao, 1985). All TI values less than zero indicate the predominance of type III kerogen in the Mouye-1 well from the Shanxi and Taiyuan shales. The measured and calculated average  $R_o$  values (Jarvie et al., 2001) are 3.35% and 3.54% for the Shanxi and Taiyuan formations, respectively. The extremely high thermal maturities show that shale samples from the Shanxi and Taiyuan formations are in the dry gas

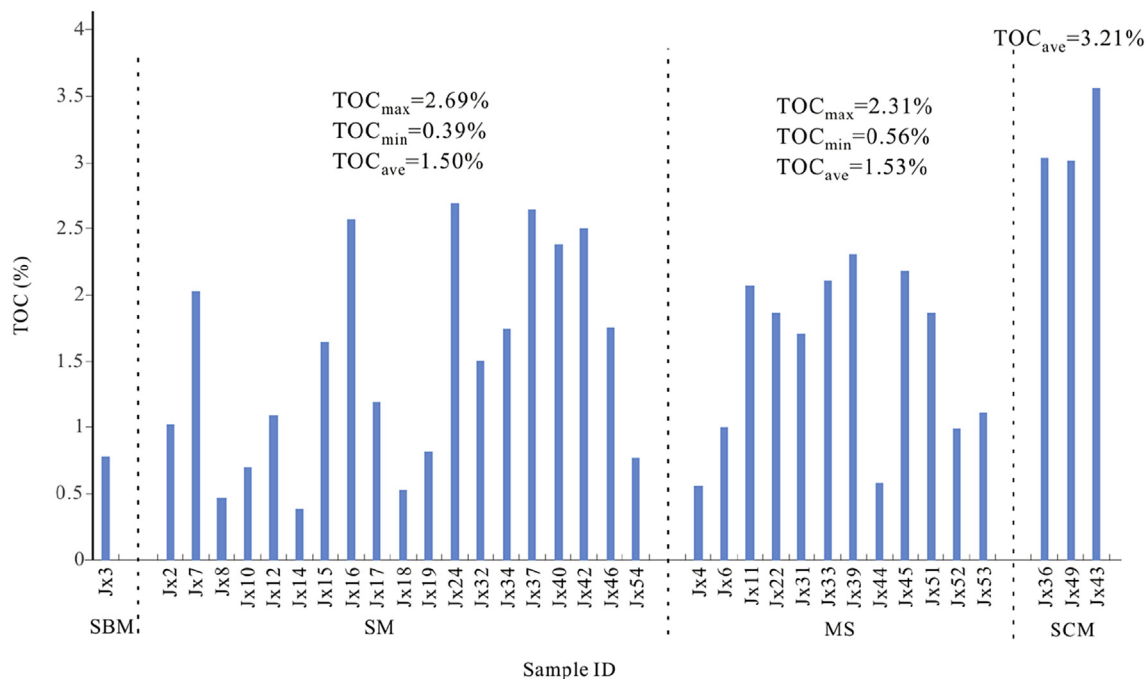


Fig. 5. Histogram of TOC (wt. %) for different lithofacies-SBM, SM, MS and SCM core samples collected from the Mouye-1 well. TOC<sub>max</sub>: Maximum value of TOC content; TOC<sub>min</sub>: Minimum value of TOC content; TOC<sub>ave</sub>: Average value of TOC content. SBM has the lowest TOC content, SM and MS have relatively higher TOC content, and SCM has the highest TOC content.

**Table 2**  
Rock-Eval, Vitrinite Reflectance and maceral composition data for the Shanxi and Taiyuan formations.

Sample	Depth (m)	Formation	S1(mg/g)	S2(mg/g)	Tmax(°C)	Ro Calc. (%)	Ro Meas. (%)	Maceral composition			TI	Kerogen Type
								Liptinite(%)	Vitrinite(%)	Inertinite(%)		
JX2	2804.81	P <sub>1s</sub>	0.07	0.4	597	3.59	3.34	0.0	22.4	77.6	-94	III
JX3	2807.74	P <sub>1s</sub>	0.03	0.02	565	3.01	3.02	0.0	77.0	23.0	-81	III
JX4	2810.32	P <sub>1s</sub>	0.06	0.14	576	3.21	3.20	0.0	94.4	5.6	-76	III
JX6	2815.3	P <sub>1s</sub>	0.02	0.14	586	3.39						
JX7	2819.27	P <sub>1s</sub>	0.01	0.56	597	3.59						
JX8	2821.74	P <sub>1s</sub>	0.03	0.11	562	2.96						
JX10	2827.13	P <sub>1s</sub>	0.02	0.09	584	3.35	3.35	64.0	6.0	30.0	-3	III
JX11	2830.72	P <sub>1s</sub>	0.05	0.77	590	3.46						
JX12	2831.66	P <sub>1s</sub>	0.03	0.16	581	3.3						
JX14	2838.32	P <sub>1s</sub>	0.03	0.08	571	3.12						
JX15	2840.23	P <sub>1s</sub>	0.02	0.22	589	3.44						
JX16	2841.88	P <sub>1s</sub>	0.09	0.47	598	3.6	3.47	0.0	13.8	86.2	-97	III
JX17	2844.32	P <sub>1s</sub>	0.07	0.24	580	3.28						
JX18	2847.16	P <sub>1s</sub>	0.03	0.09	550	2.74						
JX19	2848.82	P <sub>1s</sub>	0.02	0.1	578	3.24						
JX22	2852.36	P <sub>1s</sub>	0.05	0.25	579	3.26	3.57	5.6	11.1	83.3	-89	III
JX24	2857.02	P <sub>1s</sub>	0.03	0.34	596	3.57	3.55	0.0	14.3	85.7	-96	III
JX31	2884.3	P <sub>1s</sub>	0.06	0.18	590	3.46	3.58	11.1	5.6	83.3	-82	III
JX32	2886.27	P <sub>1s</sub>	0.01	0.03	579	3.26	3.46	36.9	10.5	52.6	-42	III
JX33	2889.34	P <sub>1s</sub>	0.03	0.1	597	3.59	3.55	6.5	7.0	86.6	-89	III
JX34	2894.31	P <sub>1s</sub>	0.13	0.23	580	3.28						
JX36	2913.2	P <sub>1t</sub>	0.05	0.24	586	3.39						
JX37	2917.42	P <sub>1t</sub>	0.04	0.16	460	1.12						
JX39	2923	P <sub>1t</sub>	0.04	0.19	600	3.64						
JX40	2925.92	P <sub>1t</sub>	0.03	0.21	588	3.42	3.58	0.0	7.5	92.5	-98	III
JX42	2931.5	P <sub>1t</sub>	0.02	0.1	597	3.59	3.59	5.9	11.7	82.4	-88	III
JX43	2933.86	P <sub>1t</sub>	0.02	0.21	599	3.62						
JX44	2935.4	P <sub>1t</sub>	0	0.01	486	1.59						
JX45	2939.27	P <sub>1t</sub>	0.07	0.21	577	3.23	3.56	0.0	16.1	83.9	-96	III
JX46	2941.28	P <sub>1t</sub>	0.03	0.18	600	3.64	3.50	34.3	6.9	58.8	-47	III
JX49	2948.32	P <sub>1t</sub>	0.04	0.09	591	3.48	3.51	0.0	66.7	33.3	-83	III
JX51	2953.09	P <sub>1t</sub>	0.03	0.18	596	3.57	3.46	0.0	15.3	84.7	-96	III
JX52	2955.71	P <sub>1t</sub>	0.03	0.1	456	1.05						
JX53	2958.16	P <sub>1t</sub>	0.02	0.06	590	3.46	3.48	0.0	17.5	82.5	-96	III
JX54	2960.13	P <sub>1t</sub>	0.03	0.03	589	3.44	3.34	0.0	36.8	63.2	-91	III

P<sub>1s</sub>: Lower Permian Shanxi formation; P<sub>1t</sub>: Lower Permian Taiyuan formation.

S1 = volatile hydrocarbon content (mg HC/g Rock); S2 = remaining hydrocarbon content (mg HC/g Rock); Ro Calc. (%) = 0.0180\*Tmax-7.16 (Jarvie et al., 2001); Ro Meas. (%) from experiment measurement.

TI = type index = 100 × (sapropelinite, %) + 50 × (liptinite, %) - 75 × (vitrinite, %) - 100 × (inertinite, %); TI ≥ 80, 80 > TI > 40, 40 > TI > 0 and TI < 0 indicate type I, type II<sub>1</sub>, type II<sub>2</sub> and type III, respectively.

**Table 3**  
TOC content, porosity, main mineralogical components and nitrogen gas adsorption data from selected core samples of different lithofacies in the Shanxi and Taiyuan formations.

Sample	Depth (m)	Formation	Lithofaciation	TOC		Porosity (%)	Total Quartz (%)	Total Carbonate (%)	Total Clay (%)	Clay Composition(%)				Nitrogen Gas Adsorption		
				(%)	(%)					Illite	Kaolinite	Chlorite	Illite/Smectite	S <sub>BET</sub> (m <sup>2</sup> /g)	V <sub>BH</sub> (cm <sup>3</sup> /g)	D <sub>ave</sub> (nm)
JX3	2807.74	P <sub>1s</sub>	SBM	0.8	2.8	24	0	76	8	51	17	24	10.87653	0.01409	5.18319	
JX8	2821.74	P <sub>1s</sub>	SM	0.5	3.4	41	0	59	39	20	13	28	4.3821	0.01243	11.3484	
JX10	2827.13	P <sub>1s</sub>	SM	0.7	2.6	34	0	66	22	35	15	28	8.87993	0.01802	8.11912	
JX12	2831.66	P <sub>1s</sub>	SM	1.1	2.8	40	0	60	46	6	4	44	5.38828	0.01596	11.36038	
JX14	2838.32	P <sub>1s</sub>	SM	0.4	2.9	43	0	57	46	22	12	20	7.05188	0.01929	10.94132	
JX16	2841.88	P <sub>1s</sub>	SM	2.6	3.0	46	0	54	39	21	13	27	5.7883	0.01365	9.43463	
JX18	2847.16	P <sub>1s</sub>	SM	0.5	2.7	47	0	53	49	15	9	27	-	-	-	
JX34	2894.31	P <sub>1s</sub>	SM	1.8	4.3	37	3	60	68	4	5	23	18.63866	0.01093	2.3462	
JX40	2925.92	P <sub>1t</sub>	SM	2.4	2.3	45	1	54	77	14	9	0	13.3191	0.03689	10.7557	
JX42	2931.5	P <sub>1t</sub>	SM	2.5	2.8	32	2	66	35	24	12	29	6.65556	0.01716	9.93474	
JX54	2960.13	P <sub>1t</sub>	SM	0.8	1.0	43	1	56	63	3	2	32	16.93858	0.03055	6.82884	
JX4	2810.32	P <sub>1s</sub>	MS	0.6	2.7	53	0	47	21	40	20	19	11.49467	0.02806	9.52309	
JX31	2884.3	P <sub>1s</sub>	MS	1.7	1.0	59	0	41	90	4	6	0	-	-	-	
JX33	2889.34	P <sub>1s</sub>	MS	2.1	4.3	57	0	43	92	3	5	0	-	-	-	
JX39	2923	P <sub>1t</sub>	MS	2.3	1.6	52	1	47	76	13	11	0	6.94731	0.00983	3.85586	
JX44	2941.28	P <sub>1t</sub>	MS	0.6	2.8	55	0	45	35	19	10	36	-	-	-	
JX52	2955.71	P <sub>1t</sub>	MS	1.0	4.5	61	7	32	38	20	14	28	10.54496	0.02599	9.35684	
JX36	2913.2	P <sub>1t</sub>	SCM	3.0	4.1	46	1	53	48	20	14	18	26.52571	0.05279	7.96079	

P<sub>1s</sub>: Lower Permian Shanxi formation; P<sub>1t</sub>: Lower Permian Taiyuan formation.

window (Tissot and Welte, 1984). This observation is further supported by previous studies, which report that abnormally high thermal maturities (>3.0%) occur in this area, primarily caused by thermal events (Xu et al., 2005, 2011; Zhao et al., 2011; Cheng et al., 2011; Wu et al., 2015). Moreover, these high temperature events within the study area may accelerate the thermal maturation of organic matter and thus shorten the hydrocarbon generation process due to the time-temperature relationship in oil/gas genesis (Connan, 1974; Dang et al., 2016).

#### 4.3. Pore characterization

Eighteen samples representing a wide range of mineral

compositions and TOC contents (Table 3), were selected from the Lower Permian Shanxi and Taiyuan Formations to explore the pore-fracture system, including pore type, porosity magnitude, pore size distribution and specific surface area.

##### 4.3.1. Pore types

BIB-SEM observations on the Taiyuan and Shanxi Formation shales identified the primary pore types, including inorganic mineral pores containing interparticle mineral pores (Fig. 6a), intercrystalline mineral pores (Fig. 6b and c) and secondary denudation pores (Fig. 6d and e); however, organic-matter pores (Fig. 6f) were rarely apparent.

In SEM images of all samples, the mineral matrix pores are

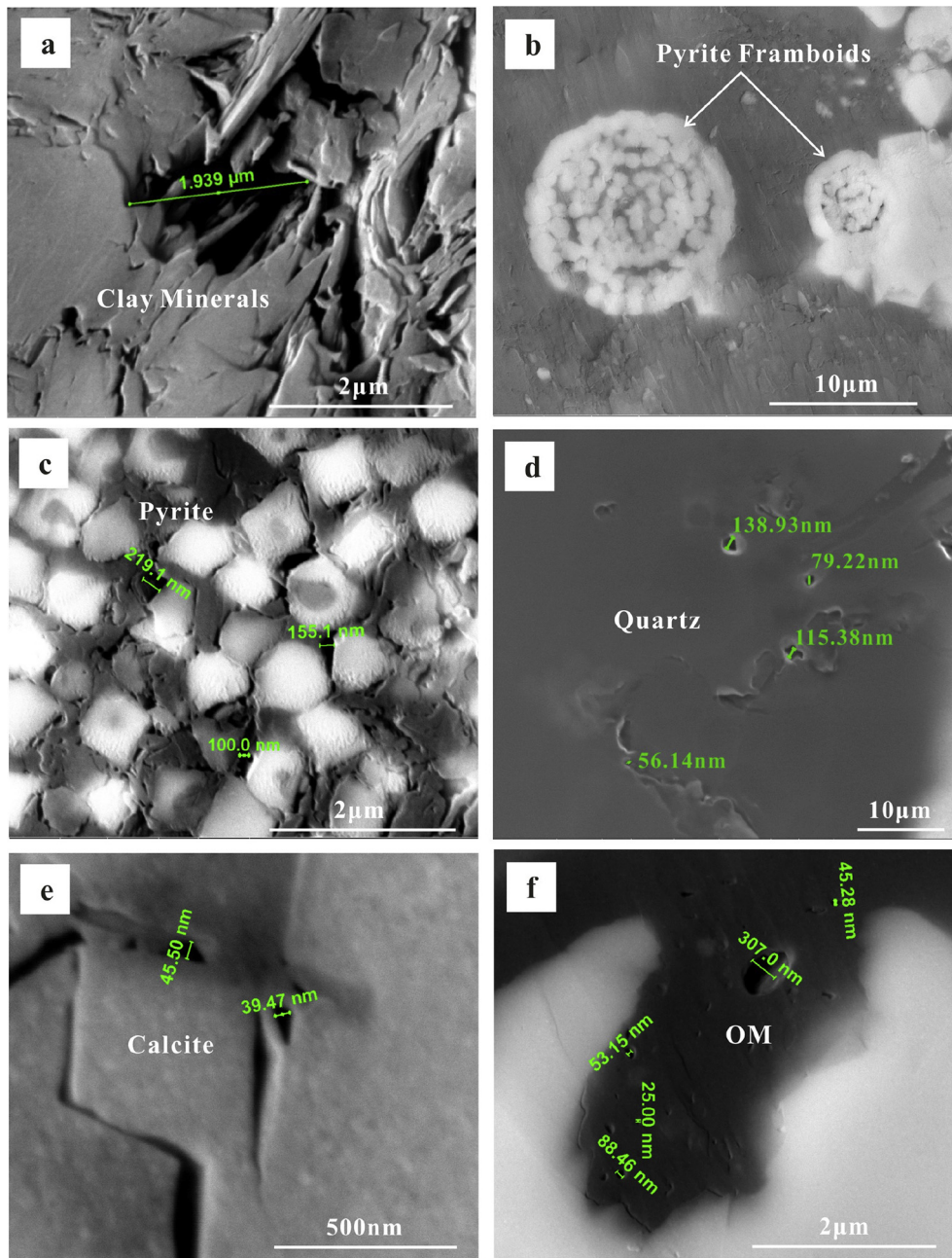


**Fig. 6.** Argon ion-milled backscatter SEM images of pores developed in Shanxi and Taiyuan shale samples: (a) interparticle pores between clay mineral floccules; (b) pyrite framboids; (c) intercrystalline pores between pyrite crystallite; (d) dissolution pores on the surface of quartz; (e) moldic pores around calcite; (f) cryptoexplosive pores associated with organic matter hydrocarbon generation; OM = organic matter.

primarily observed between and within clay (Fig. 6a) and pyrite framboids (Fig. 6b and c), representing interparticle mineral pores and intercrystalline mineral pores, respectively. Additionally, some secondary dissolution pores are also within the quartz matrix (Fig. 6d) and along the margins of calcite (Fig. 6e) - usually developed under deep burial. The mineral components of the Shanxi and Taiyuan shales are primarily comprised of clay and quartz group minerals. The ductile minerals consist of clay floccules and organic matter, whereas brittle minerals primarily contain quartz, feldspar and authigenic pyrite. All of the minerals experienced a large number of micro-sedimentary structural movements, incomplete cementation between various particles, and late-diagenetic transformation generating intergranular pores. These inorganic mineral pores are primarily associated with sizes ranging from tens to more than one hundred nanometers, providing the storage space for the shale gas in the study area.

A few organic-matter pores are also found in the form of cryptoexplosive pores caused by the process of kerogen cracking to hydrocarbon (Fig. 6f). Although such organic-matter pores are very few in number, they document the historical generation of hydrocarbon.

#### 4.3.2. Pore microstructure

N<sub>2</sub>GA analysis was successfully performed on 14 samples that varied widely in TOC contents and mineral composition (Table 3). Both adsorption and desorption isotherms were obtained to document the hysteresis loop and to preliminarily identify the pore

types. The isotherms of four representative samples from different lithofacies are shown in Fig. 7. All of the isotherms show a hysteric pattern, but do not show a horizontal plateau at high relative pressure close to unity. This indicates that the signal is an ensemble of a variety of curve types rather than any single IUPAC classification group (Sing et al., 1985). Samples JX3 (SBM) and JX36 (SCM) have high relative adsorbance and display similar isotherms. High adsorbance is exhibited at a low relative pressure, indicating that the facies contain micropores (Type I). The hysteresis loop at higher relative pressures ( $P/P_0 > 0.2$ ) indicates the multilayer range associated with capillary condensation in mesopores (Type IV). Additionally, the observation that the isotherms are still hyperbolic at relative pressures close to unity reveals the existence of macropores (Ravikovitch and Neimark, 2002). Samples JX34 (SM) and JX39 (MS) have relatively low adsorbed amounts and show a similar isothermal shape that mixes the Type III and Type IV physisorption isotherms. In these samples, the initial adsorption is extremely low - indicating non-micropores or very few micropores. The hysteresis loop patterns at a higher relative pressure ( $P/P_0 > 0.2$ ) and hyperbolic isotherms ( $P/P_0 \approx 1$ ) are also indicative of mixtures of mesopores and macropores in the samples (Fig. 7). The reversible adsorption-desorption process, characterized by the presence of hysteresis loops, suggests that pores within the samples are open and connected. Parallel-plate (slit-) type pores appear to be the dominant pore type in the samples as inferred from further analysis of the curve separation gradient (Ruthven, 1984; Horvath and Kawazoe, 1983; Ravikovitch and Neimark, 2002).

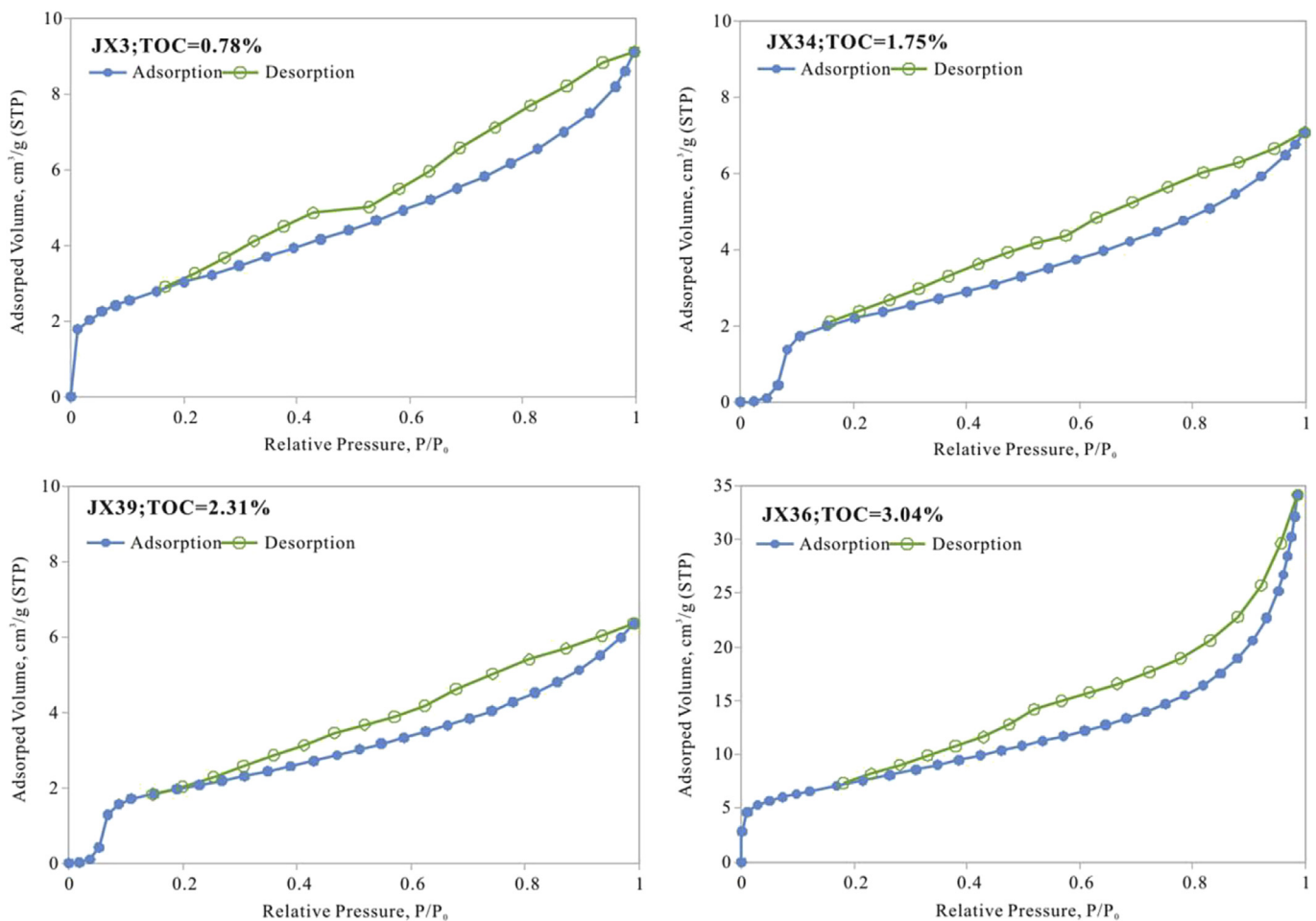


Fig. 7. Nitrogen gas adsorption and desorption isotherms for four representative core samples at 77 K.

### 4.3.3. Porosity

Based on the qualitative descriptions of the pore types provided by SEM images, a quantitative calculation of porosity was derived from the difference between the bulk and grain densities (Chalmers et al., 2012a) and is shown in Table 3. The measured samples exhibit porosities between 1% and 4.5%, which is within the porosity range of North American shales (Chalmers et al., 2012a,b; Hao and Zou, 2013). SCM has the highest porosity, averaging 4.1%, with the other three lithofacies presenting similar average porosities of ~2.8%. All of the samples contain the same Type III kerogen and equivalent vitrinite reflectances ranging from 3.02% to 3.8%, with an average of 3.45%. This represents humic-type organic matter and implies thermal over-maturity (Table 2). This excludes the effect of maturation on porosity development.

## 5. Discussion

### 5.1. Shale composition and porosity

The measured samples exhibit porosities between 1% and 4.5% (Table 3). Among the four lithofacies, SCM holds the highest porosity, averaging 4.1%, and the other three lithofacies present similar average porosities of ~2.8%. Positive correlations exist between porosity and both the kaolinite and chlorite contents (inorganic minerals), and negative correlations occur with the illite content (Fig. 8). Porosity and the TOC content are poorly correlated (Fig. 8). This may indicate that there is a more significant contribution of inorganic mineral pores to overall porosity compared to the contribution of organic pores. This is consistent with the SEM observations. By contrast, the Mississippian Barnett shale of the

Fort Worth Basin, Texas, which has numerous nano-scale micropores, displays a significant contribution of over 75% of pores in organic matter (Loucks et al., 2012). This may imply that there are more large pores, such as meso- and/or macropores, in the Lower Permian Shanxi and Taiyuan Formation transitional shales due to the higher contribution of inorganic mineral pores. Of course, the validity of this assumption requires further investigation.

Such a conclusion is also supported by the geochemical information. The organic matter in the core samples has a uniform characterization as a Type III kerogen representing thermal over-maturation. When  $R_o$  reaches a maximum, the pores in the organic matter will disappear due to the stronger effect of compaction. Additionally, organic pores may develop in different organic macerals, and Type III kerogen is always enriched with large amounts of vitrinites that are less prone to developing organic pores. Thus, pores in organic-matter are rare.

### 5.2. Lithofacies and pore microstructure

To investigate the distribution and contribution of each pore, the pore volume and specific surface area with respect to the PSD are determined from the adsorption branches of the BJH model (Barret et al., 1951; Houben et al., 2013). The pore sizes range from 0.35 to 500 nm, including micropores, mesopores and partial macropores. This is consistent with the interpretation of hysteresis loop-type models. As illustrated in Fig. 9, the plot of  $dV/dD$  versus  $D$  shows that the majority of pores have diameters <10 nm (typically 2 nm–10 nm) and the concentration of pores decreases with an increase in pore size. However, as shown in the plot of  $dV/d\log(D)$ , most curves display two peak pore size ranges, indicating that

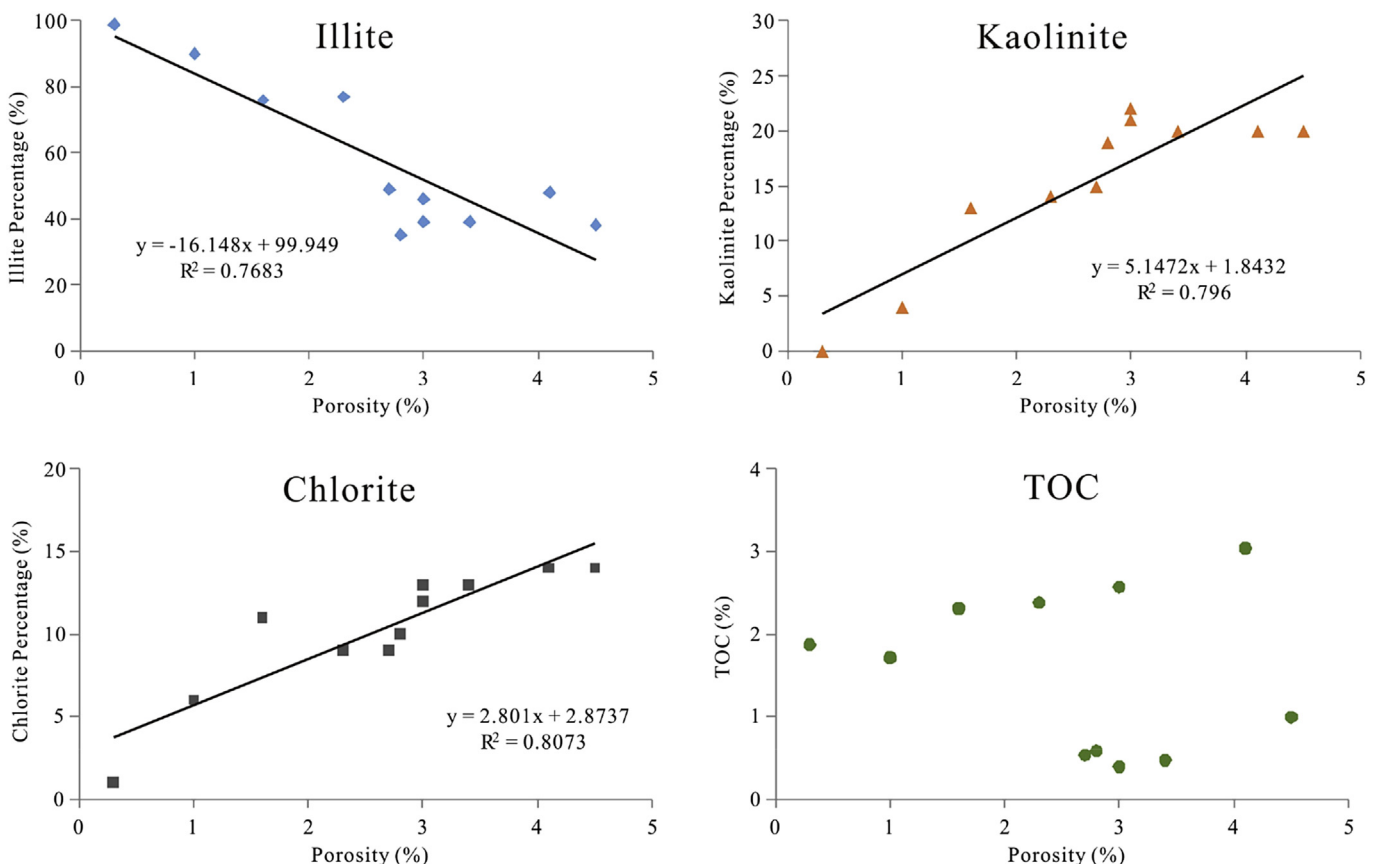


Fig. 8. Correlations between shale mineralogical components and porosity.

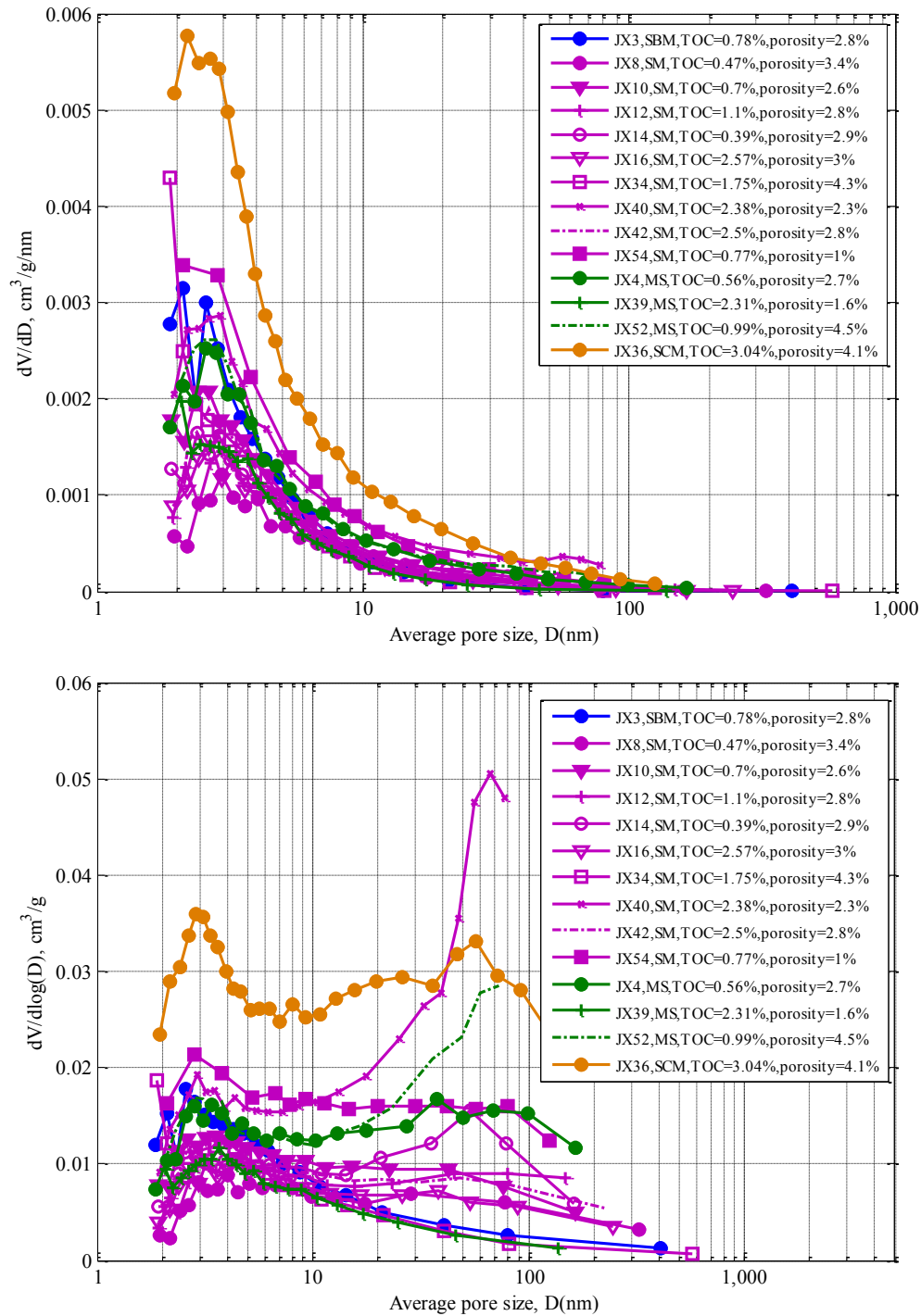


Fig. 9. Pore volume distributions with pore sizes derived from nitrogen gas adsorption isotherms using the BJH model.

larger pores, with diameters of 50–100 nm, also contribute significantly to the total pore volume. This suggests that the volume of large pores is many times greater than the volume of small pores. The distribution of the specific surface with respect to pore size reveals that the specific surface areas are primarily controlled by smaller pores (Fig. 10).

Such a conclusion is also consistent with the observation from Fig. 11, which compares the relative contribution of micropores (<2 nm), mesopores (2–50 nm) and macropores (>50 nm) to the

total pore volume and specific surface area. That is, mesopores and macropores primarily contribute to the total pore volume. However, the specific surface area is controlled by relatively smaller pores (micropores and mesopores) (Fig. 11). This is also supported by the evidence from many gas shales in North American basins (Chalmers and Bustin, 2007a,b; Chalmers and Bustin, 2008; Ross and Bustin, 2009). Thus, it follows that mesopores with moderate pore sizes play an important role in pore development. In the study area, SCM with the highest porosity has the largest volume, specific

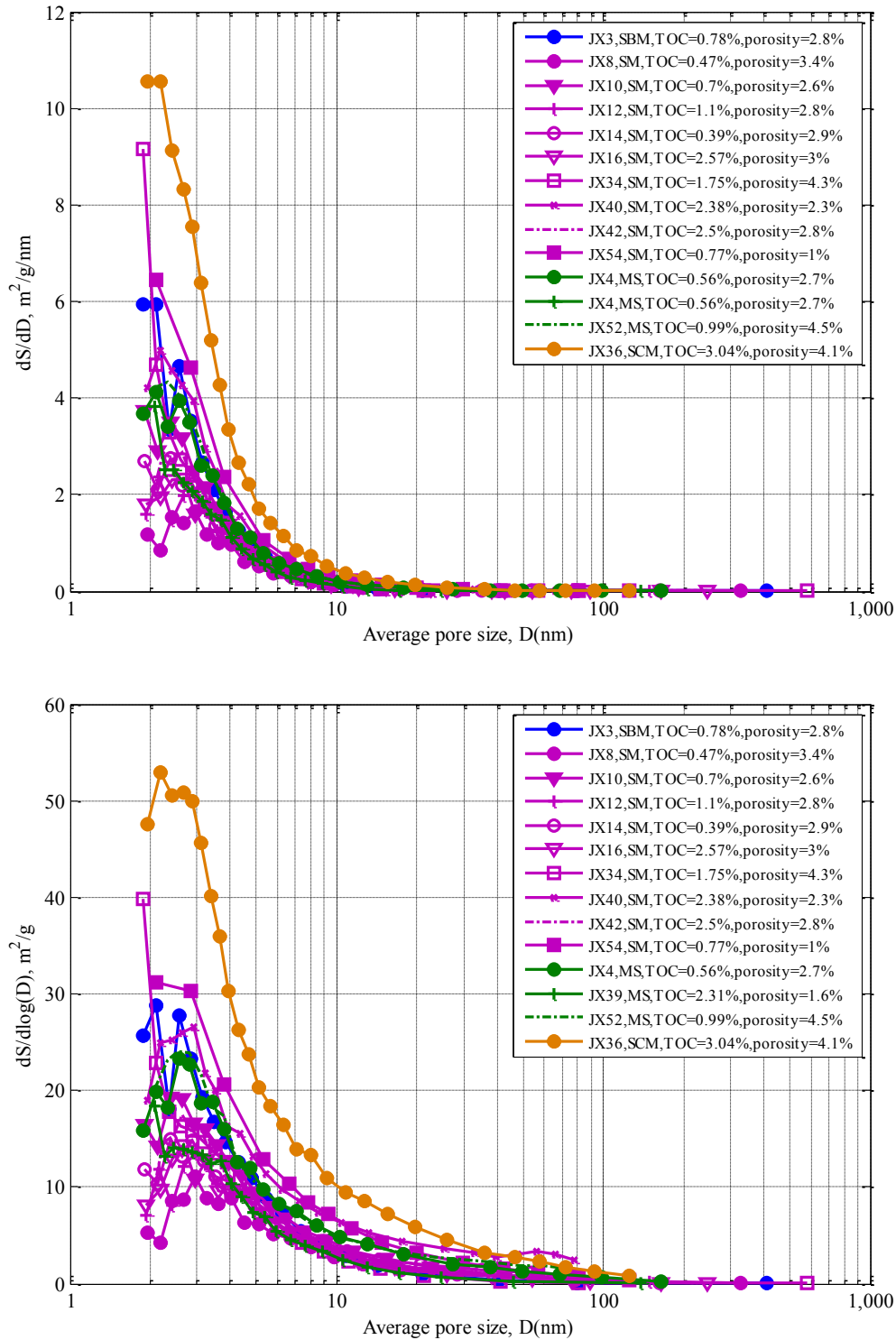


Fig. 10. Specific surface area distributions with pore sizes derived from nitrogen gas adsorption isotherms using the BJH model.

surface area and adsorption amount (Figs. 6–8), as well as the highest TOC content. This may indicate the existence of many more mesopores. This type of lithofacies could be considered to be favorable for shale-gas production in the Lower Permian Shanxi and Taiyuan Shales (via Mouye-1 well). Of course, the geo-mechanical parameters from further investigation are also required to corroborate this suggestion.

### 5.3. Petrophysics

The Th/U ratio can be used as a chemostratigraphic method for determining whether ancient marine, continental regimes, or both influenced the depositional cycles associated with lithological strata (Adams and Weaver, 1958). As shown in the spectral gamma-ray log data in Fig. 2, the Th/U ratios are dominantly >7, indicating

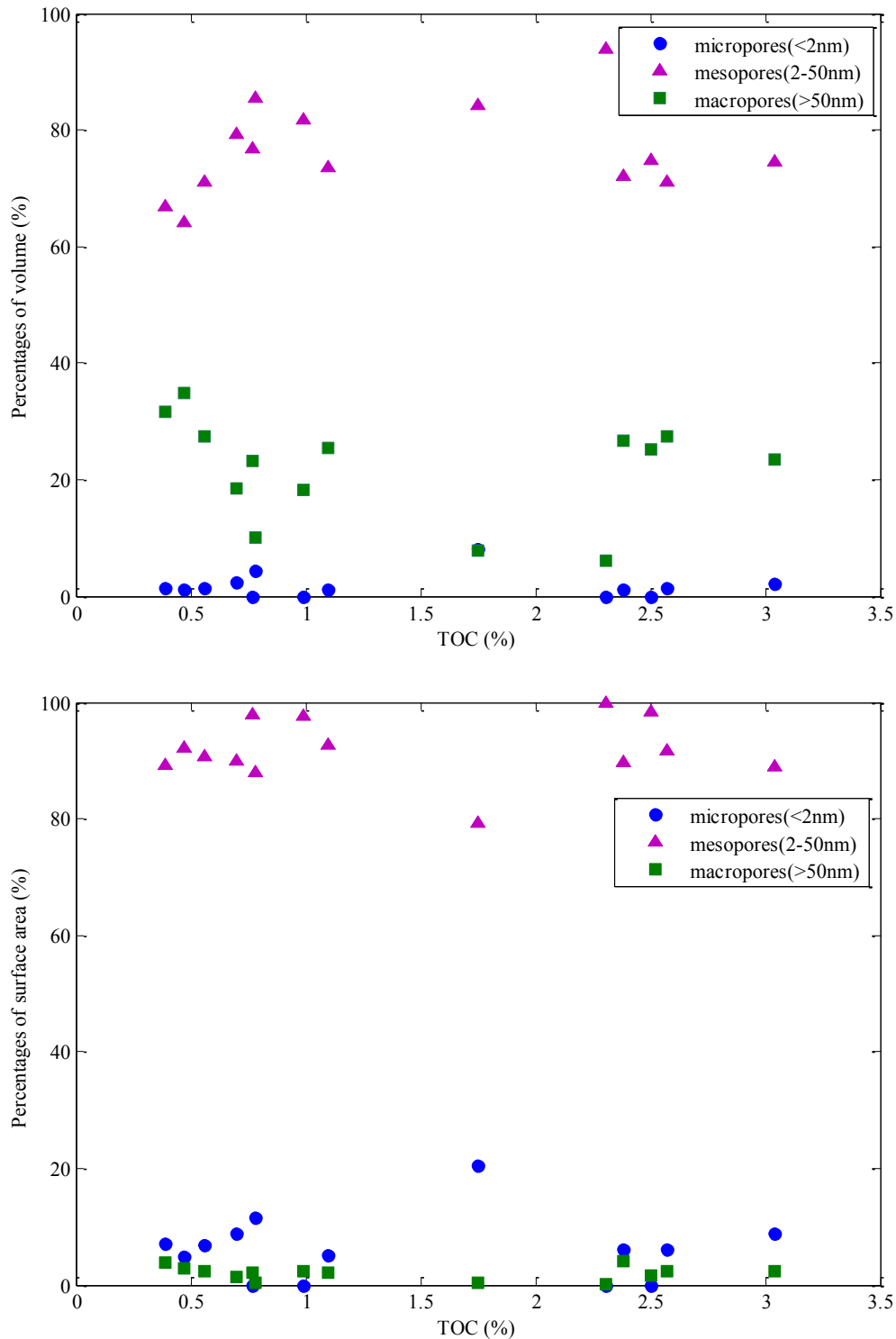


Fig. 11. Plot showing the relative contributions of micropores, mesopores and macropores to the total volume and total surface area.

oxidized continental deposits. Some intervals also exhibit a Th/U ratio between 2 and 7, which is representative of a marine sedimentary environment with a minor terrigenous supply. This is significantly different from the lower Barnett presented in Fig. 7. The Th/U ratios of the lower Barnett are almost all <2, a value that Adams and Weaver (1958) suggests is characteristic of a marine origin.

A comparison of the Th/U ratio and U logging curves for the

lower Permian Shanxi and Taiyuan shales against lower Barnett shales (Figs. 2 and 12) shows a similar trend in sea level changes. That is, a sudden spike in uranium followed by a gradual decline, which may be related to a gradual regression of the sea and sea level. The observed gradual increase in the Th/U ratio, coupled with the drop in uranium through the section may mark basinal changes in anoxia due to low-stands in sea level. For the lower Barnett shales, the high sea level, with relatively low Th/U ratios

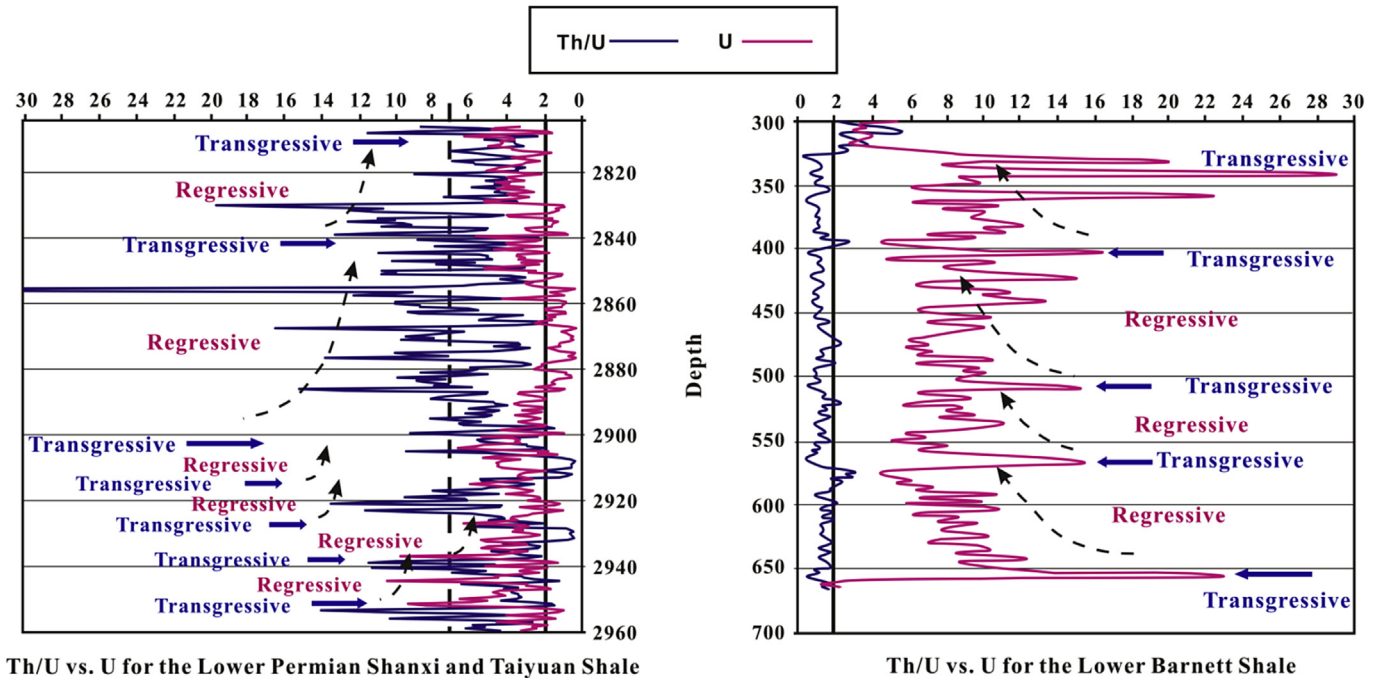


Fig. 12. Plots of Th/U versus U for the Lower Permian Shanxi and Taiyuan Shale and the Lower Barnett shale (modified from Jacobi et al., 2008).

Table 4

Geomechanical parameters derived from triaxial compression tests on selected core samples of different lithofacies in the Shanxi and Taiyuan formations.

Sample	Lithofacies	Young's Modulus (GPa)	Poission's Rate	YM <sub>BI</sub> (%)	PR <sub>BI</sub> (%)	BI (%)
JX3	SBM	9.01	0.22	-1.41	72.00	35.29
JX4	MS	9.39	0.18	-0.87	88.00	43.56
JX6	MS	15.19	0.21	7.41	76.00	41.71
JX22	MS	11.19	0.24	1.70	64.00	32.85
JX31	MS	24.58	0.21	20.83	76.00	48.41
JX33	MS	11.69	0.18	2.41	88.00	45.21
JX39	MS	38.68	0.21	40.97	76.00	58.49
JX44	MS	26.49	0.23	23.56	68.00	45.78
JX52	MS	23.43	0.23	19.19	68.00	43.59
JX53	MS	20.17	0.15	14.53	100.00	57.26
JX8	SM	13.36	0.19	4.80	84.00	44.40
JX10	SM	15.65	0.24	8.07	64.00	36.04
JX12	SM	13.10	0.18	4.43	88.00	46.21
JX14	SM	18.83	0.20	12.61	80.00	46.31
JX16	SM	24.83	0.23	21.19	68.00	44.59
JX18	SM	19.01	0.23	12.87	68.00	40.44
JX34	SM	25.14	0.19	21.63	84.00	52.81
JX40	SM	30.69	0.22	29.56	72.00	50.78
JX42	SM	23.27	0.20	18.96	80.00	49.48
JX54	SM	26.02	0.19	22.89	84.00	53.44
JX36	SCM	31.18	0.20	30.26	80.00	55.13
JX43	SCM	24.10	0.19	20.14	84.00	52.07
JX49	SCM	27.18	0.23	24.54	68.00	46.27

BI=Brittleness Index=(YM<sub>BI</sub> + PR<sub>BI</sub>)/2; YMBI=(YM-1)/(8-1) × 100%; PRBI= (PR-0.4)/(0.15-0.4) × 100% (Rickman et al., 2008).

YM=Young's Modulus, 10 GPa; PR=Poission's Ratio; YM<sub>BI</sub> = binned Young's Modulus, PR<sub>BI</sub> = binned Poission's Ratio.

corresponding to intervals often containing an elevated phosphatic content, clay, and the highest TOC (Kochenov and Baturin, 2002), is often the preferred target zone (Jarvie et al., 2005). However, this principle is not applicable to lower Permian Shanxi and Taiyuan shales. As displayed in Fig. 2, the highest sea level with the lowest Th/U ratio corresponds to the carbonate lithofacies in the Taiyuan formation. Carbonate lithofacies is considered to be an undesirable target due to the difficulty in propagating fracture networks, with anisotropies due to natural fractures, karsting, and cavernous porosity (Johnston, 2004; Jarvie et al., 2007). Thus, for fracturing

transitional shales, characterization of the Th/U logging data analysis should be addressed differently due to the frequently changing lithofacies and sedimentary environments. Note that a favorable fracturing target should be optimized by integrating the lithological characteristics with a relatively low Th/U zone, though not necessarily the lowest Th/U section.

#### 5.4. Shale fracability evaluation

The concept of rock brittleness has been introduced to help

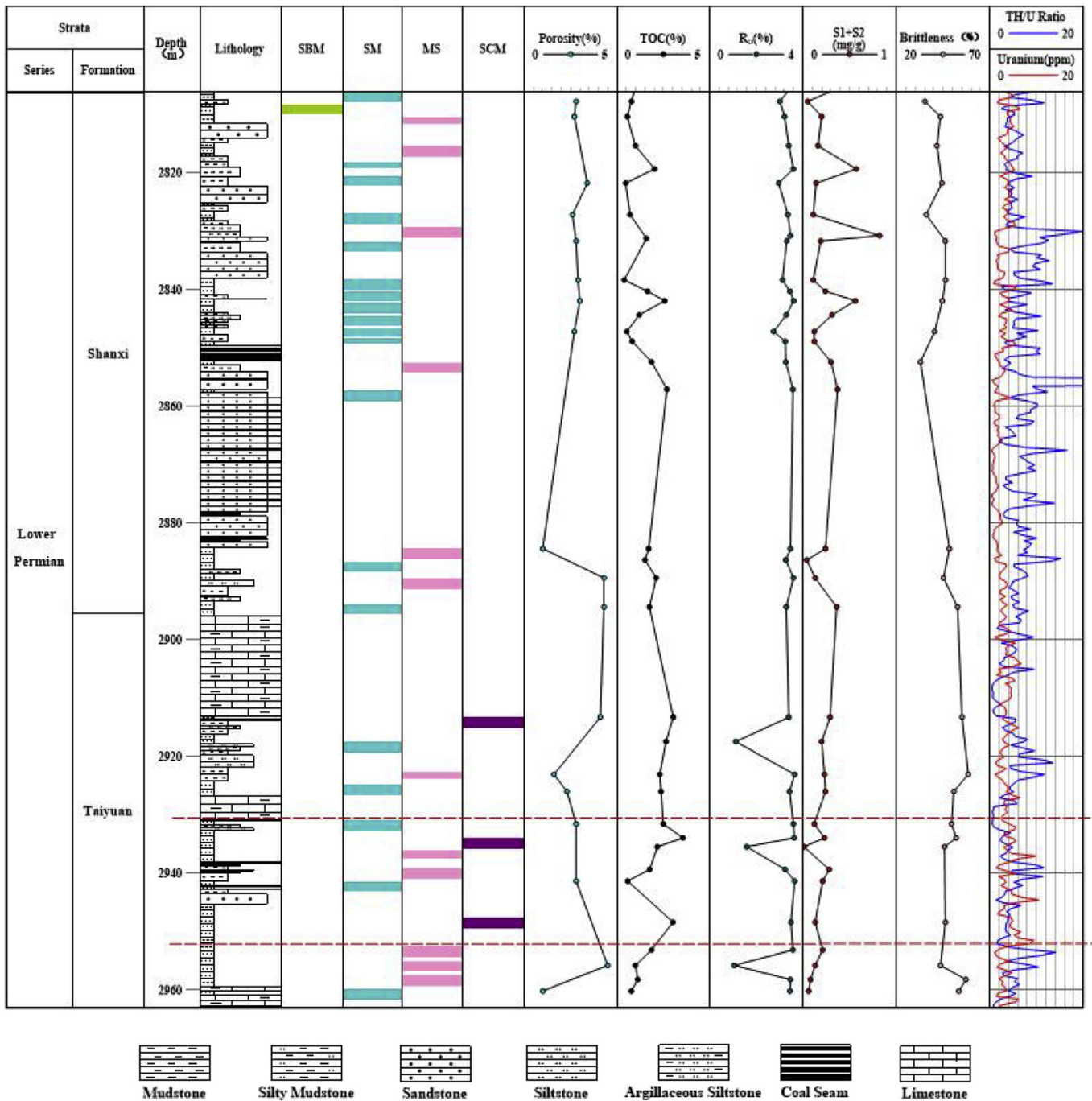


Fig. 13. Stratigraphic column representing TOC, porosity,  $R_o$ , gas potential, brittleness and spectral gamma-ray log data for the Lower Permian Shanxi and Taiyuan formation.

evaluate shale fracability. This concept combines both Young's Modulus and Poisson's Ratio. These two components are integrated to reflect the ability of the rock to fail under applied stress (Poisson's Ratio) and to maintain the resulting fracture (Young's Modulus) once it is formed (Rickman et al., 2008). It can be concluded from the brittleness index calculation (Rickman et al., 2008) that the smaller the Poisson's Ratio and larger the Young's Modulus, the more brittle the rock. Britt and Schoeffler (2009) posited that the prospective shale should have a Young's Modulus in excess of 23.8 GPa. The Poisson's ratios and Young's Modulus of the measured samples derived from the triaxial compression tests are listed in Table 4, together with the calculated brittleness index.

SCM exhibits the highest brittleness index, averaging 51%; MS and SM have similar BI, with an average of ~46%, while SBM has the lowest BI. In addition, the Young's Modulus of the SCM samples are all greater than 23.8 GPa, with an average of 27.49 GPa, while the average moduli are less than 21 GPa for the three other lithofacies. Thus, in this study area, SCM, as a brittle shale, is more likely to respond well to hydraulic fracturing treatments.

There are several other criteria to define the likely success of shales as successful gas plays. These include a moderate shale thickness (>20 m), high thermal maturity (1.2–3.5% $R_o$ ) and high TOC content (>2%) (Charpentier and Cook, 2011; Gross et al., 2015). Based on these criteria, combined with the results from the above

investigation, we optimize the most desired fracturing zone between the two red dashed lines shown in Fig. 13. This is within the Taiyuan Shale at a depth of 2930–2952 m, which contains more MSC with a higher porosity, TOC, S1+S2, and brittleness and a lower Th/U value. Taiyuan Shale has the highest shale gas potential and can be regarded as the desired target in the study area.

## 6. Conclusions

Transitional shales of the Lower Permian Shanxi and Taiyuan formations in the sNCB (collected from the Mouye-1 well) are comprehensively examined to define the lithofacies and pore characteristics and to link these criteria to optimize target zones for shale gas production. The following preliminary conclusions can be drawn:

- (1) A total of four lithofacies were identified, including silt bearing mudstone (SBM), silty mudstone (SM), muddy siltstone (MS) and silty carbonaceous mudstone (SCM). SCM has both the highest TOC content and porosity.
- (2) Interparticle mineral pores, intercrystalline mineral pores, secondary dissolution pores and relatively few pores in the organic matter comprise the pore system in the Lower Permian Shanxi and Taiyuan shales. In particular, the inorganic mineral pores are the most fully developed and provide the principal storage volume for gas. Pores within the organic-matter are seldom observed, potentially due to the nature of the vitrinite-rich Type III kerogen.
- (3) The pore microstructure of the shales is rather complex with a broad pore size distribution involving micropores, mesopores and macropores (derived from nitrogen gas adsorption). The total pore volume is contributed predominantly by larger pores, while the specific surface area is primarily contributed by smaller pores, such as meso-/micropores. In this study area, silty carbonaceous mudstone has the greatest potential for shale gas residing in the abundant mesopores.
- (4) Based on the integrated criteria, the Taiyuan Shale section presents at a depth of 2930–2952 m and is the most promising target in the study area. This zone contains more MSC, with a high porosity, TOC, S1+S2, and brittleness and a low Th/U value.

## Acknowledgements

The authors are grateful to Henan Yukuang Geological Exploration & Investment Co., Ltd. for access to core samples and permission to publish this paper. Special thanks to the support from the China Scholarship Council (CSC) and College of Earth and Mineral Sciences of the Pennsylvania State University.

## References

- Adams, J.A., Weaver, C.E., 1958. Thorium-to-uranium ratios as indicators of sedimentary processes: example of concept of geochemical facies. *AAPG Bull.* 42 (2), 387–430.
- Akatsuka, K., 2000. 3-D Geological Modeling of a Carbonate Reservoir, Utilizing Open-hole Log Response-porosity & Permeability-lithofacies Relationship. 9th Abu Dhabi International Petroleum Exhibition and Conference, Abu Dhabi, United Arab Emirates. October 13–15, 2000, SPE Paper 87239 (11 pp.).
- Aplin, A.C., Macquaker, J.H.S., 2011. Mudstone diversity: origin and implications for source, seal, and reservoir properties in petroleum systems. *AAPG Bull.* 95 (12), 2031–2059.
- Barret, E.P., Joyner, L.G., Halenda, P.P., 1951. The determination of pore volume and area distribution in porous substances. I. Computations from nitrogen isotherms. *J. Am. Chem. Soc.* 73 (1), 373–380.
- Berteig, V., Helgeland, J., Mohn, E., Langeland, T., vander Wel, D., 1985. Lithofacies Prediction from Well Data. Transactions of the 26th Society of Petrophysicists and Well Log Analysts Annual Logging Symposium, Dallas, Texas. June 17–20, (25 pp.).
- Boyer, C., Kieschnick, J., Suarez-Rivera, R., Lewis, R.E., Waters, G., 2006. Producing gas from its source. *Oilfield Rev.* 18 (3), 36–49.
- Bridge, J.S., Jalfin, G.A., Georgieff, S.M., 2000. Geometry, lithofacies, and spatial distribution of Cretaceous fluvial sandstone bodies, San Jorge Basin, Argentina: outcrop analog for the hydrocarbon-bearing Chubut Group. *J. Sediment. Res.* 70 (2), 341–359.
- Britt, L.K., Schoeffler, J., 2009. The Geomechanics of a Shale Play: what Makes a Shale Prospective. SPE Eastern Regional Meeting, Charleston, West Virginia, USA, pp. 23–25. September, SPE Paper 125525 (9 pp.).
- Brunauer, S., Emmett, P.H., Teller, E., 1938. Adsorption of gases in multimolecular layers. *J. Am. Chem. Soc.* 60 (2), 309–319.
- Bustin, R.M., Bustin, A.M.M., Cui, X., Ross, D.J.K., Pathi, M., 2008. Impact of Shale Properties on Pore Structure and Storage Characteristics. SPE Shale Gas Production Conference, Fort Worth, Texas, USA. November 16–18, 2008, SPE Paper 119892 (28 pp.).
- Cao, Q.Y., 1985. Identification of microcomponents and types of kerogen under transmitted light. *Petroleum Explor. Dev.* (05), 14–23.
- Chalmers, G.R.L., Bustin, R.M., 2007a. On the effects of petrographic composition on coalbed methane sorption. *Int. J. Coal Geol.* 69 (4), 288–304.
- Chalmers, G.R.L., Bustin, R.M., 2007b. The organic matter distribution and methane capacity of the Lower Cretaceous strata of Northeastern British Columbia, Canada. *Int. J. Coal Geol.* 70 (1), 223–339.
- Chalmers, G.R.L., Bustin, R.M., 2008. Lower Cretaceous gas shales in northeastern British Columbia, part I: geological controls on methane sorption capacity. *Bull. Can. Petroleum Geol.* 56 (1), 1–21.
- Chalmers, G.R.L., Bustin, R.M., Power, I.M., 2012a. Characterization of gas shale pore systems by porosimetry, surface area, and field emission scanning electron microscopy/transmission electron microscopy image analysis: examples from the Barnett, Woodford, Haynesville, Marcellus, and Doing units. *AAPG Bull.* 96 (6), 1099–1119.
- Chalmers, G.R.L., Ross, D.J.K., Bustin, R.M., 2012b. Geological controls on matrix permeability of Devonian gas shales in the horn river and liard basins, northeastern British Columbia, Canada. *Int. J. Coal Geol.* 103, 120–131.
- Charpentier, R.R., Cook, T.A., 2011. USGS Methodology for Assessing Continuous Petroleum Resources. U.S. Geological Survey Open-File Report, 2011-1167.
- Chen, J.P., Zhao, C.Y., He, Z.H., 1997. Criteria for evaluating the hydrocarbon generating potential of organic matter in coal measures. *Petroleum Explor. Dev.* 1, 1–5.
- Cheng, Z., Xu, X.H., Wang, R.X., Wu, M.H., Xin, L.L., 2011. Reasons for abnormal thermal evolution of source rocks in Upper Paleozoic, southern North China. *Petroleum Geol. Exp.* 33 (2), 142–147.
- Connan, J., 1974. Time-temperature relation in oil genesis: geologic notes. *AAPG Bull.* 58 (12), 2516–2521.
- Curtis, J.B., 2002. Fractured shale-gas systems. *AAPG Bull.* 86 (11), 1921–1928.
- Curtis, M.E., Ambrose, R.J., Sondergeld, C.H., Rai, C.S., 2010. Structural Characterization of Gas Shale on the Micro- and Nano-scale. Canadian Unconventional Resources and International Petroleum Conference, Calgary, Alberta, Canada. October 19–21, 2010, SPE Paper 137693 (15pp.).
- Curtis, M.E., Sondergeld, C.H., Ambrose, R.J., Rai, C.S., 2012. Micro-structural investigation of gas shales in two and three dimensions using nanometer-scale resolution imaging. *AAPG Bull.* 96 (4), 665–677.
- Dang, W., Zhang, J.C., Tang, X., Chen, Q., Han, S.B., Li, Z.M., Du, X.R., Wei, X.L., Zhang, M.Q., Liu, J., Peng, J.L., Huang, Z.L., 2016. Shale gas potential of Lower Permian marine-continental transitional black shales in the Southern North China Basin, central China: characterization of organic geochemistry. *J. Nat. Gas Sci. Eng.* 28, 639–650.
- Ding, W.L., Zhu, D.W., Cai, J.J., Gong, M.L., Chen, F.Y., 2013. Analysis of the developmental characteristics and major regulating factors of fractures in marine-continental transitional shale-gas reservoirs: a case study of the Carboniferous-Permian strata in the southeastern Ordos Basin, central China. *Mar. Petroleum Geol.* 45, 121–133.
- Dong, C.M., Ma, C.F., Lin, C.Y., Sun, X., Yuan, M.Y., 2015. A method of classification of shale set. *J. China Univ. Petroleum Ed. Nat. Sci.* 39 (3), 1–7.
- Gasparik, M., Bertier, P., Gensterblum, Y., Ghanizadeh, A., Krooss, B.M., Littke, R., 2014. Geological controls on the methane storage capacity in organic-rich shales. *Int. J. Coal Geol.* 123, 34–51.
- GB/T19145-2003, 2003. Determination of Total Organic Carbon in Sedimentary Rock. Standardization Administration of the People's Republic of China.
- GB/T19587-2004, 2004. Determination of the Specific Surface Area of Solids by Gas Adsorption Using the BET Method. Standardization Administration of the People's Republic of China.
- Gross, D., Sachsenhofer, R.F., Bechtel, A., Pytlak, L., Rupprecht, B., Wegerer, E., 2015. Organic geochemistry of Mississippian shales (Bowland Shale Formation) in central Britain: implications for depositional environment, source rock and gas shale potential. *Mar. Petroleum Geol.* 59, 1–21.
- Hao, F., Zou, H., 2013. Cause of shale gas geochemical anomalies and mechanisms for gas enrichment and depletion in high-maturity shales. *Mar. Petroleum Geol.* 44, 1–12.
- Hill, R.J., Zhang, E., Katz, B.J., Tang, Y., 2007. Modeling of gas generation from the Barnett shale, Fort Worth Basin, Texas. *AAPG Bull.* 91 (4), 501–521.
- Horvath, G., Kawazoe, K., 1983. Method for the calculation of effective pore size distribution in molecular sieve carbon. *J. Chem. Eng. Jpn.* 16 (6), 470–475.
- Hou, D.J., Feng, Z.H., 2011. Oil and Gas Geochemistry. Petroleum Industry Press.
- Houben, M.E., Desbois, G., Urai, J.L., 2013. Pore morphology and distribution in the shaly facies of Opalinus Clay (Mont Terri, Switzerland): insights from

- representative 2D BIB-SEM investigations on mm to nm scale. *Appl. Clay Sci.* 71, 82–97.
- Huang, Z.G., Gao, C.L., Ji, R.S., 2005. Analysis of evolution of Meso-Cenozoic basins in southern North China. *Oil Gas Geol.* 26, 252–256.
- Jacobi, D.J., Gladkikh, M., LeCompte, B., Hursan, G., Mendez, F., Longo, J., Ong, S., Bratovich, M., Patton, G.L. and Shoemaker, P., Integrated petrophysical evaluation of shale gas reservoirs, 2008, CIPC/SPE Gas Technology Symposium 2008 joint Conference, Calgary, Alberta, Canada, June 16–19, 2008, SPE Paper 114925(23 pp).
- Jarvie, D., Lundell, L., 1991. Hydrocarbon Generation Modeling of Naturally and Artificially Matured Barnett Shale, Fort Worth Basin, Texas: Southwest Regional Geochemistry Meeting, September 8–9, 1991, The Woodlands, Texas, 1991.
- Jarvie, D.M., Brenda, L.C., floyd, B.H., John, T.B., 2001. Oil and Shale Gas from the Barnett Shale, Ft. Worth Basin, Texas. *AAPG Bulletin*, 10, A100.
- Jarvie, D.M., Hill, R.J., Pollastro, R.M., 2005. Assessment of the gas potential and yields from shales: the Barnett Shale model. *Okla. Geol. Surv. Circ.* 110, 37–50.
- Jarvie, D.M., Hill, R.J., Ruble, T.E., Pollastro, R.M., 2007. Unconventional shale-gas systems: the Mississippian Barnett Shale of north-central Texas as one model for thermogenic shale-gas assessment. *AAPG Bull.* 91 (4), 475–499.
- Javadpour, F., 2009. Nanopores and apparent permeability of gas slow in mudrocks (shales and siltstones). *J. Can. Petroleum Technol.* 48 (8), 16–21.
- Johnston, D., 2004. Technological advances expand potential play. *Oil Gas J.* 102 (3), 51–51.
- Klaver, J., Desbois, G., Urai, J.L., Littke, R., 2012. BIB-SEM study of the pore space morphology in early mature Posidonia Shale from the Hils area, Germany. *Int. J. Coal Geol.* 103, 12–25.
- Klaver, J., Desbois, G., Littke, R., Urai, J.L., 2015. BIB-SEM characterization of pore space morphology and distribution in postmature to overmature samples from the Haynesville and Bossier Shales. *Mar. petroleum Geol.* 59, 451–466.
- Kochenov, A.V., Baturin, G.N., 2002. The paragenesis of organic matter, phosphorus, and uranium in marine sediments. *Lithology Mineral Resour.* 37 (2), 107–120.
- Kuila, U., Prasad, M., 2013. Specific surface area and pore-size distribution in clays and shales. *Geophys. Prospect.* 61 (2), 341–362.
- Ling, Z.B., Zou, D.B., Zhang, K., Xu, M., Wang, J., 2011. Investigation on measuring methodology of rock and ore sample porosity. *J. Jilin Univ. (Earth Sci. Ed.)* 41 (3), 921–924.
- Loucks, R.G., Reed, R.M., Ruppel, S.C., Jarvie, D.M., 2009. Morphology, genesis, and distribution of nanometer-scale pores in siliceous mudstones of the Mississippian Barnett Shale. *J. Sediment. Res.* 79 (12), 848–861.
- Loucks, R.G., Reed, R.M., Ruppel, S.C., Hammes, U., 2012. Spectrum of pore types and networks in mudrocks and a descriptive classification for matrix-related mudrock pores. *AAPG Bull.* 96 (6), 1071–1098.
- Lv, J.X., Huang, Z.G., Zhai, C.B., 2005. Formation settings of the Mesozoic and Cenozoic basins in the southern part of North China. *Petroleum Geol. Exp.* 27 (2), 118–123.
- Mastalerz, M., He, L., Melnichenko, Y.B., Rupp, J.A., 2012. Porosity of coal and Shale: insights from gas adsorption and SANS/USANS techniques. *Energy & Fuels* 26 (8), 5109–5120.
- Mayka, S., Celso, P.F., José, A.B., da Cunha Neto, Fabiano, G.W., Viviane, S.S. dos Santos, 2013. Characterization of pore systems in seal rocks using nitrogen gas adsorption combined with mercury injection capillary pressure techniques. *Mar. Petroleum Geol.* 39 (1), 138–149.
- Milliken, K., Rudnicki, M., Awwiller, D.N., Zhang, T., 2013. Organic matter-hosted pore system, marcellus formation (devonian), Pennsylvania. *AAPG Bull.* 97 (2), 177–200.
- Mitra, A., Warrington, D.S., Sommer, A., 2010. Application of Lithofacies Models to Characterize Unconventional Shale Gas Reservoirs and Identify Optimal Completion Intervals. SPE Western Regional Meeting, Anaheim, California, USA, May 27–29, 2010, SPE Paper 132513 (9 pp.).
- Nelson, P.H., 2009. Pore-throat sizes in sandstones, siltstones and shale. *AAPG Bull.* 93 (3), 329–340.
- Porta, G.D., Kenter, J.A.M., Immenhauser, A., Bahamonde, J.R., 2002. Lithofacies character and architecture across a pennsylvanian inner-platform transect (sierra de cuera, asturias, Spain). *J. Sediment. Res.* 72 (6), 898–916.
- Qi, L., Carr, T.R., 2006. Neural network prediction of carbonate lithofacies from well logs, Big Bow and Sand Arroyo Creek fields, southwest Kansas. *Comput. Geosciences* 32 (7), 947–964.
- Qi, L., Carr, T.R., Goldstein, R.H., 2007. Geostatistical three-dimensional modeling of oolite shoals, St. Louis Limestone, southwest Kansas. *AAPG Bull.* 91 (1), 69–96.
- Qin, J.Z., 2005. Hydrocarbon Source Rocks in China. Science Press, Beijing, 2005.
- Ravikovich, P.I., Neimark, A.V., 2002. Experimental confirmation of different mechanisms of evaporation from ink-bottle type pores: equilibrium, pore blocking, and cavitation. *Langmuir* 18 (25), 9830–9837.
- Rickman, R., Mullen, M.J., Petre, J.E., Grieser, W.V., Kundert, D., 2008. A Practical Use of Shale Petrophysics for Stimulation Design Optimization: All Shale Plays Are Not Clones of the Barnett Shale. SPE Annual Technical Conference and Exhibition, Denver, Colorado, USA, September 21–24, 2008, SPE Paper 115258 (11 pp.).
- Ross, D.J.K., Bustin, R.M., 2009. The importance of shale composition and pore structure upon gas storage potential of shale gas reservoirs. *Mar. Petroleum Geol.* 26 (6), 916–927.
- Ruthven, D.M., 1984. Principles of Adsorption and Adsorption Processes. Wiley, New York.
- Sing, K.S., Everett, D.H., Haul, R.A.W., Moscou, L., Pierotti, R.A., Rouquerol, J., Siemieniewska, T., 1985. Reporting physisorption data for gas/solid systems with special reference to the determination of surface area and porosity. *Pure Appl. Chem.* 57 (4), 603–619.
- Sun, Z.M., 1996. Tectonic evolution and petroleum exploration prospective of Tai-kang uplift. *Petroleum Explor. Dev.* 23 (5), 6–10+81.
- SY/T5124-1995, 1995. Method for Determining the Vitrinite Reflectance in the Sedimentary Rocks. China Petroleum Standardization Committee.
- SY/T5125-1996, 1996. Identification and Classification Method of the Maceral Composition of Organic Matter Using Fluorescence-fluorescent Light. China Petroleum Standardization Committee.
- SY/T5163-2010, 2010. The X-ray Diffraction (XRD) Analysis Method for Clay Minerals and Common Non-clay Minerals in the Sedimentary Rocks. China Petroleum Standardization Committee.
- SY/T5368-2000, 2000. Thin Section Examination of Rock. China Petroleum Standardization Committee.
- SY/T6154-1995, 1995. Determination of Rock Specific Surface and Pore Size Distribution by Static Nitrogen Adsorption. China Petroleum Standardization Committee.
- Tian, H., Pan, L., Xiao, X.M., Ronald, W.T.W., Meng, Z.P., 2013. A preliminary study on the pore characterization of Lower Silurian black shales in the Chuandong Thrust Fold Belt, southwestern China using low pressure N<sub>2</sub> adsorption and FE-SEM methods. *Mar. Petroleum Geol.* 48, 8–19.
- Tissot, B.P., Welte, D.H., 1984. Petroleum Formation and Occurrence, pp. 131–170.
- Wang, G.C., Carr, T.R., 2012. Methodology of organic-rich shale lithofacies identification and prediction: a case study from Marcellus Shale in the Appalachian basin. *Comput. Geosciences* 49, 151–163.
- Wang, D.Y., Tang, X.Y., Chen, N.M., 1994. Structural features, evolution and oil and gas prospects of Kai Feng Depression. *ACTA PET. SIN.* 15 (2), 39–47.
- Wang, J., Gao, L.Y., Ling, Z.B., Zhang, X., 2005. A new method of density measurement for rock and ore materials. *Prog. Geophys.* 20 (2), 440–442.
- Wong, P.M., Gedeon, T.D., Taggart, I.J., 1995. The Use of Fuzzy ARTMAP for Lithofacies Classifications: a Comparison Study. Transactions of the 36th Society of Petrophysicists and Well Log Analysts Annual Logging Symposium, Paris, France, June 26–29, (12 pp.).
- Wu, Y., Fan, T.L., Zhang, J.C., Jiang, S., Li, Y.F., Zhang, J.P., Xie, C., 2014. Characterization of the upper ordovician and lower silurian marine shale in northwestern guizhou Province of the upper yangtze block, south China: implication for shale gas potential. *Energy & Fuels* 28 (6), 3679–3687.
- Wu, W., Wang, Y.H., Cao, G.S., Huang, X.F., Liu, W.Q., 2015. The geochemical characteristics of the carboniferous and permian source rocks in the Western Henan, the southern North China basin. *Nat. Gas. Geosci.* 26 (1), 128–136.
- Xu, H.L., Zhao, Z.J., Lu, F.L., Yang, Y., Tang, Z., Sun, G., Xu, Y., 2004. Tectonic evolution of the nanhuabei area and analysis about its petroleum potential. *Geotect. Metallogenia* 28 (4), 450–463.
- Xu, H.Z., Hu, Z.Q., Zhou, X.K., Wang, C.G., 2005. Lower Paleozoic hydrocarbon-generation history in the mid-south of North China basin. *Acta Pet. Sin.* 26 (1), 31–37.
- Xu, X.H., Chen, X.J., Lei, M., Li, S.J., Zhou, X.J., Wu, M.H., 2011. Exploration prospects of the carboniferous and permian in the southern North China. *Petroleum Geol. Exp.* 33 (2), 148–154.
- Yang, C., Zhang, J.C., Li, W.J., Jing, T.Y., Sun, R., Wang, Z.P., He, W., Lu, Y.Y., 2014. Microscopic pore characteristics of Sha-3 and Sha-4 shale and their accumulation significance in Liaohe Depression. *Oil Gas Geol.* 35 (2), 286–294.
- Yang, X.Q., Fan, T.L., Wu, Y., 2016. Lithofacies and cyclicity of the lower cambrian niutitang shale in the mayang basin of Western hunan, south China. *J. Nat. Gas Sci. Eng.* 28, 74–86.
- Yao, T., Chopra, A., 2000. Integration of seismic attribute map into 3D facies modeling. *J. Petroleum Sci. Eng.* 27 (1), 69–84.
- Yu, H.Z., Lu, F.L., Guo, Q.X., Lu, W.Z., Wu, J.Y., Han, S.H., 2005. Proto-sediment basin types and tectonic evolution in the southern edge of North China Plate. *Petroleum Geol. Exp.* 27 (2), 111–117.
- Zeng, X.L., Liu, S.G., Huang, W.M., Zhang, C.J., 2012. Comparison of silurian longmaxi Formation shale of sichuan basin in China and carboniferous Barnett Formation shale of Fort Worth Basin in United States. *Geol. Bull. China* 30 (2/3), 372–384.
- Zhang, J.C., Jin, Z.J., Yuan, M.S., 2004. Reservoiring mechanism of shale gas and its distribution. *Nat. Gas. Ind.* 24 (7), 14–18.
- Zhang, J.C., Xu, B., Nie, H.K., Wang, Z.Y., Lin, T., 2008. Exploration potential of shale gas resource in China. *Nat. Gas. Ind.* 28 (6), 136–140.
- Zhao, J.F., Liu, C.Y., Liu, Y.T., He, Z.G., Mao, W., Zhu, B., 2011. Reconstruction of thermal evolutionary history of the Upper Paleozoic in the southern North China. *Oil Gas Geol.* 32 (1), 64–74.
- Zou, C.N., Dong, D.Z., Wang, S.J., Li, J.Z., Li, X.J., Wang, Y.M., Li, D.H., Cheng, K.M., 2010. Petroleum Explor. Dev. 37 (6), 641–653.